A MEMS Magnetic-Based Vibrational Energy Harvester

by

Abraham Shin

Submitted to the Department of Electrical Engineering and Computer Science
in partial fulfillment of the requirements for the degree of

Master of Engineering in Electrical Engineering

at the

MASSACHUSETTS INSTITUTE OF TECHNOLOGY

June 2018

Author .....
Department of Electrical Engineering and Computer Science
May 25, 2018

Certified by .....
Jeffrey H. Lang
Professor of Electrical Engineering and Computer Science
Thesis Supervisor

Accepted by .....
Katrina LaCurts
Chair, Master of Engineering Thesis Committee

A MEMS Magnetic-Based Vibrational Energy Harvester

by

Abraham Shin

Submitted to the Department of Electrical Engineering and Computer Science
on May 25, 2018, in partial fulfillment of the
requirements for the degree of
Master of Engineering in Electrical Engineering

Abstract

This thesis presents the design, fabrication, and testing of a MEMS vibration energy harvester that is to operate at low frequency to power machine health monitoring. The energy harvester converts external vibration into electricity via the Lorentz-force by allowing a permanent magnet, which acts as an inertial mass, to oscillate between coils wound above and below the magnet. Careful analysis and design of a fabricated silicon-based suspension, which holds the magnet, determines the important mechanical properties of the harvester, such as the internal loss and the selectivity of a single translational vibration. The harvester is designed to provide maximum power output at 0.5 g external acceleration at 50 Hz while its size is constrained to be less than 1 cm^3. By incorporating mechanical and electromagnetic analyses, a full-system optimization is performed to determine the optimal dimensional parameters of the harvester and to estimate the power output to be observed. The fabricated and assembled energy harvester is tested and observed to produce an open-circuit voltage of 100 mV and a power output of 165 μW at the resonance frequency of 45.7 Hz. The harvester's power density is 382 $\mu W/cm^3$, which is higher than the highest reported value of 222$\mu W/cm^3$ for existing MEMS energy harvesters, but the performance of the design presented in this thesis may be improved with some changes to the current design.

Thesis Supervisor: Jeffrey H. Lang
Title: Professor of Electrical Engineering and Computer Science

Acknowledgments

I thank my parents for providing me with unwavering support and the opportunity to pursue my education and achieve my goals. I also thank my sister for her advice and presence.

I thank Professor Jeffrey H. Lang for guiding me throughout the years, teaching me perseverance in the face of challenges, and inspiring me with his unyielding dedication. I thank Professor Anantha Chandrakasan for his support and allowing the device to be assembled and tested in his laboratory.

I thank Mr. Dennis Ward for fabricating the MEMS suspensions and taking SEM pictures shown in the paper. I thank Mr. Mark Belanger for his support in producing tools and various parts of the harvester. I thank Ruize Xu at MIT for providing the vibrating platform.

Finally, I thank Ujwal Radhakrishna for showing me his passion for research and helping me with his wisdom and expertise.

Contents

List of Figures

List of Tables

Chapter 1

Introduction

Harvesting energy from ambient sources, such as sunlight, wind, and waves, is an active field of research. Large scale harvesting of alternative energy, in particular, has been and continues to be a main focus in progressing towards a more sustainable living.[1] On the other end, the increasing demand to power Micro Electronic Mechanical System (MEMS) applications, such as autonomous sensors and wearable devices, has fueled a demand fo,r and development of, micro-scale energy harvesting.[2]

Over the past few decades, advancements in technology have allowed MEMS devices to continue to decrease in size, improving the devices' spatial utility while lowering the cost of material.[4] To take advantage of these achievements, MEMS devices must be integrated with a reliable and robust power supplies whose sizes are comparable to the devices they power.[5] These requirements have pushed researchers to convert ambient energy into electricity using MEMS energy harvesters, which have theoretically infinite energy production and a volume that varies between 0.01 cm^2 and 10 cm^2. These are stark improvements from conventional batteries, which hold a limited amount of energy and have volumes that are a few orders of magnitude higher than the MEMS devices they aim to charge. Further considering that disposed batteries are hazardous to the environment, the need to replace batteries with energy harvesters has become increasingly important.

This thesis focuses on the design and fabrication of a MEMS harvester that harnesses ambient vibration energy to produce an alternating current that can charge

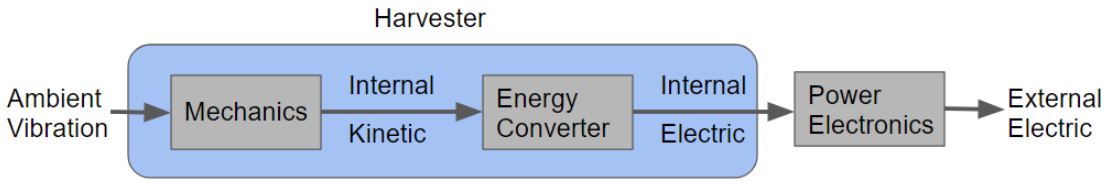

Figure 1-1: Systemic View of a Vibration Energy Harvester

an energy store or power a MEMS device for machine health monitoring. In general, a vibration harvester converts external vibration into internal kinetic energy with a suspension that couples the external oscillation with an internal movement. The internal kinetic energy can then be converted into electrical energy in the form of a voltage difference or electric current. A separate power electronics circuit captures and regulates the incoming electrical signal into a steady, controlled electrical energy that can be stored or sourced to a device in need of power. A system view of a vibration harvester is shown in Figure 1-1, where the harvester's domain is indicated in the blue box.

Additional specifications that dictate the design of the harvesters are employed here for a general application of various MEMS devices. Under the assumption that most devices and machines operate at a fundamental frequency in the range of 45 - 60 Hz, the harvester needs to be able to produce electrical energy in that range of frequencies. For convenience of design, however, the resonance frequency of the suspension inside the harvester is designed to optimally covert the external vibration into internal kinetic energy under the vibrational frequency of 50 Hz, approximately the geometric mean of 45 and 60 Hz. The amplitude of the external vibration is chosen to be 0.5 g, which corresponds to approximately 5 m/s^2. For this device to have a size that is comparable to other MEMS devices, its volume is restricted to be 1 cm^3 at maximum.[2] Finally, the harvester must provide at least 100 µW. This is a generic set of specifications to guide the upcoming analysis and design of the harvester to accommodate for machine health monitoring applications.

To satisfy the above specifications, the product should be a high-power integrated harvester. To optimize for the power density, as measured in power output per unit

volume, the harvesting scheme must be electromagnetic due to its effectiveness at small size and low frequency compared to other schemes, such as piezoelectric or variable-capaticance. The device must also be fabricated from silicon wafers to ensure that the suspension that supports the internal inertial reference is flexible and easy to fabricate.

The review paper [2] examines various electromagnetic vibration harvesters designed and tested in the last few decades. The harvesters are designed based on a diverse set of specifications. The best power density is produced by micro-cantilever beams and vertical tube harvesters, neither of which are integrated MEMS harvesters. The best harvester that focuses on compatibility with MEMS devices uses a permanent magnet mounted on a planar spring to produce 222 $\mu W/cm^3$.[3]

The goal of the design process presented in this thesis is to improve the amount of power, and power density, of the harvester compared to published designs while producing a robust and reliable device that integrates well with other MEMS applications. The results from the experiments with the finished product must also correspond to the predicted data from the analysis.

This thesis explores the design, fabrication, and testing of an electromagnetic (EM) energy harvester that sources its energy from vibrations in the environment. After this introduction, Chapter 2 compares various harvesting schemes to justify the choice of an EM harvester. Chapters 3 and 4 introduce mechanical and electromagnetic optimization analyses essential to the design. Chapter 5 explores a few suspension options for the harvester and justifies the choice of the accordion spring. All the previous analyses are combined to fully optimize the design through an iterative process and are presented in Chapter 6. Chapter 7 discusses the fabrication and assembly of the parts, which are then tested to produce the results shown in Chapter 8. Finally, a summary and conclusions, as well as suggestions for future studies, are presented in the last chapter.

Chapter 2

Preliminary Mechanical Optimization

The first step in a vibration energy harvester's operation is to convert ambient vibration energy into internal kinetic energy, which requires an inertial reference, provided by a proof mass, and a suspension. The dimensions and shape of the suspension dictate the conversion for an electromagnetic harvester. Before designing the device, a preliminary analysis of the mechanics must be performed to discern how variables, such as operating frequency, vibration amplitude, and dimensions of the center mass affect the power output given a constrained set of dimensions.

2.1 Spring, Mass, and Damper System in Suspension

As described in the previous chapter, the electromagnetic energy harvester relies on a permanent magnet's oscillation with respect to coils of wire. To encapsulate the mechanics of the suspension, the harvester can be modeled as a lossless spring-mass-damper system that is coupled with an external vibration, as is shown in Figure 2-1. The goal of this chapter is to optimize the output power with the constraints on the footprint of the entire design in mind.

In Figure 2-1, the blue box represents the harvester, which houses a proof mass, shown as a red box. The proof mass is suspended inside the harvester through a

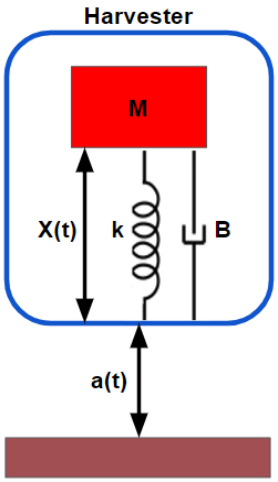

Figure 2-1: Simplified Model for the Electromagnetic Harvester in Suspension

spring and a damper, which have the spring constant k, and the damping factor B, respectively. The harvester is coupled to inertial ground by an external vibration, a(t), and the displacement of the proof mass with respect to the casing of the harvester is X(t). To clarify, a(t) is the casing vibration amplitude, which has the units of acceleration (m/s^2), and is not the same physical quantity as X(t), which is the displacement (m) of the proof mass with respect to the casing.

In the model, the spring constant is a dependent variable: the spring is chosen to set the resonance frequency of the suspension to be 50 Hz. For simplicity, the linear damper represents the conversion of energy from the mechanical system to the electrical system and can be viewed as the output of the harvester. In reality, the internal loss through mechanical friction, air drag, and back current among other dissipating factors acts as a damper that does not contribute to the output power. Therefore, a small fraction of the power output through the damper is actually the internal loss of the system.

Analyzing the model under sinusoidal steady state is another assumption that simplifies the analysis. The spectral content of most vibrating sources has widespread peaks and harmonics. Therefore, the suspension inside the harvester may not oscillate in a sinusoidal motion, but the quality factors of MEMS suspensions are high enough so that X(t) can be approximated as sinusoidal. This assumption can be checked

when the quality factor of the device is approximated in the results and later found experimentally. The displacement of the proof mass with respect to the harvester casing is $X(t) = \Re(|\hat{X}|e^{j\omega t})$, where $|\hat{X}|$ is the maximum displacement of the center mass, or the stroke of the suspension. Similarly, the vibration amplitude is expressed as $a(t) = \Re(|\hat{A}|e^{j\omega t})$, where $|\hat{A}|$ is the maximum acceleration applied to the device from its environment at the operating frequency of ω. For simplicity, $\Re()$ notation will be dropped for the rest of the analysis.

The second-order differential equation that describes the mechanical system then becomes

$$M\ddot{X} + B\dot{X} + kX = -Ma \tag{2.1}$$

Substituting the X(t) and a(t) expressions into (2.1) results in

$$(-M\omega^2 + Bj\omega + k)\hat{X}e^{j\omega t} = -M\hat{A}e^{j\omega t} \tag{2.2}$$

$$((k - M\omega^2) + jB\omega)\hat{X} = -M\hat{A} \tag{2.3}$$

If the harvester is assumed to operate under resonance frequency, $\omega = \omega_\circ = \frac{k}{M}$, (3.3) simplifies to

$$j(B\omega)\hat{X} = M\hat{A} \tag{2.4}$$

$$|X| = \frac{M|A|}{B\omega} \tag{2.5}$$

The time-averaged output power from the harvester is the amount of power transferred to the damper, $< P_d >=< B\dot{X}^2 >= \frac{1}{2}B\omega^2|\hat{X}|^2$. The power expression here is multiplied by a half because the time average of a square of a unity sinusoidal function is one half. Since the footprint, or the size, of the harvester is the main constraint in the analysis, B from the power expression is substituted using (2.5) to yield

$$< P_d >= \frac{1}{2}(\frac{Ma}{\omega_\circ|\hat{X}|})\omega_\circ^2|\hat{X}|^2 = \frac{Ma\omega_\circ|\hat{X}|}{2}. \tag{2.6}$$

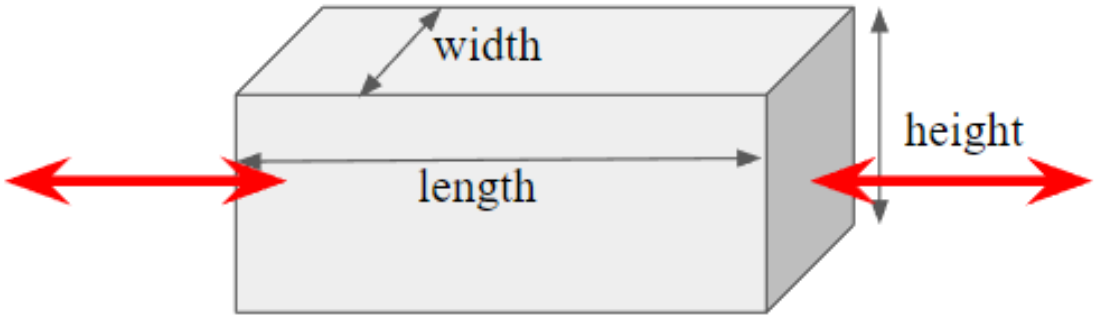

Figure 2-2: The center mass vibrating along the red arrows and its dimensions labeled

2.2 Simplified Model Analysis Results

In (2.6), the output power is directly proportional to the mass of the proof mass, external vibration amplitude, resonance frequency, and the stroke of the center mass. The vibration amplitude and resonance frequency are predefined specifications that the design does not control. The mass, which depends on the volume of the proof mass, and the stroke are independent variables that can be controlled through the structural design.

An important observation from the result is that M and $|X|$ are equally important in the output power, and both require space within the harvester. For further analysis, suppose that the proof mass is a rectangular prism with the variables l, w, and h, corresponding to the length, width, and height of the mass. The length of the mass is in the direction of its movement, the width is perpendicular to the movement from the top view, and the height is perpendicular to the movement from the side view. A diagram that shows the mass with the appropriate labeling of dimensions is shown in Figure 2-2.

A dimensional constraint on the harvester dictates that the device has a length L allotted for the combined length of the proof mass, l, and the stroke lengths on both sides of the proof mass, $2|\hat{X}|$ to account for vibration. The constraint is expressed as $L = l + 2|X|$. The power output expression in (2.6) then becomes

$$< P_d >= \frac{Ma\omega_\circ|\hat{X}|}{2} = (l \cdot w \cdot h \cdot \rho)\frac{a\omega_\circ|\hat{X}|}{2} = ((L - 2|\hat{X}|) \cdot w \cdot h \cdot \rho)\frac{a\omega_\circ|\hat{X}|}{2}, \quad (2.7)$$

where ρ is the density of the center mass. The power output is maximized when $|\hat{X}| = L/4$ and $l = L/2$. This shows that roughly half of the volume inside a harvester should be dedicated to the proof mass and the other should be used for stroke. When $|X| = L/4$ and $l = L/2$ are substituted into (3.7), the result is

$$< P_d >= (l^2wh)\frac{\rho a\omega_\circ}{4}. \quad (2.8)$$

The final expression above shows that the length of the proof mass contributes more to the output power than any other factor. The vibration of the suspension, therefore, should be in the direction of the longest dimension of the harvester. Additionally, the power is optimized not only by having a wider and taller magnet but also by increasing the density of the center mass.

In an electromagnetic harvester, alternating current is generated by having a permanent magnet and coils of wire oscillate with respect to each other to produce an alternating current by the Lorentz-force principle. The proof mass, therefore, can be a block of wound wires or a block magnet. A neodymium magnet (NdFeB Magnet) has a density that ranges between 7300 to 7500 kg/m^3 where as the density of copper, which is the main ingredient in a wire, is 8900 kg/m^3.[6] The wires have a higher density than a magnet, but a wire cannot fill the entire block with its volume. Due to the imperfect packing of a wire, its effective density as the proof mass is reduced by at least 30%, which lowers its effective density below that of the magnet. A bigger and more practical reason for using a magnet as the proof mass is the wire connection. To deliver the generated current to the power electronics, the wires must be connected to the rest of the circuit. If the wires are oscillating along with the proof mass, however, the wire connections to the proof mass need to oscillate with the mass and cause additional damping as the wire connections are bent with each period of oscillation. Therefore, a neodymium magnet should be used as the proof mass while

wires are placed above and below the magnet in the frame of the harvester housing.

2.3 Summary and Discussion

The analysis of a simplified harvester model has demonstrated that the stroke and mass of the proof mass must be as large as possible for maximum output power. Further, the direction of the mass's oscillation should be in the direction of the longest dimension of the casing. To ensure this, a neodymium block magnet is used as the proof mass and the length of the magnet is around half of the length of the harvester.

Keep in mind, however, that these results are derived from a simplified model that does not consider the effects of internal damping or the effects of loading of the harvester. The results above serve only to provide a qualitative explanation that the stroke and the mass of the magnet must both be large to provide a large output power when considering the open circuit modeling of the mechanics of the harvester. The exact ratio of the length of the magnet to the harvester must be decided after the addition of the aforementioned details into our current simplified model.

Chapter 3

Electromagnetic Analysis

The next step of energy harvesting for an electromagnetic energy harvester is the conversion of internal kinetic energy into alternating electrical current. The conversion is achieved by a magnet, or magnets, oscillating around coils of wires to generate induced voltage with which to drive a current and therefore provide power to a load. This chapter outlines the steps involved in deciding on a magnet/coil configuration as well as the electromagnetic analysis that specifies the dimensions of the harvester pertaining to the generation of electricity.

3.1 Sizing and Configuration of Magnets and Coils

To narrow down the scope of the analysis, the general configuration of the magnets and the coils are determined first. By Faraday's law, the induced voltage in a loop of wires is proportional to the rate of change in magnetic flux through the loop. The induced voltage can be maximized by increasing the change in magnetic flux and the number of turns in a loop. The simplest way to increase the change in magnetic flux is to use a strong magnet. Another way to achieve the same is to use two different magnets that are attached side-by-side with different polarities as shown in Figure 3-1 to increase the rate of change in magnetic flux.

As the pair of magnets sweep past the loops, the magnetic flux goes from positive to negative, or vice versa. For the same total volume of magnets, this is a far

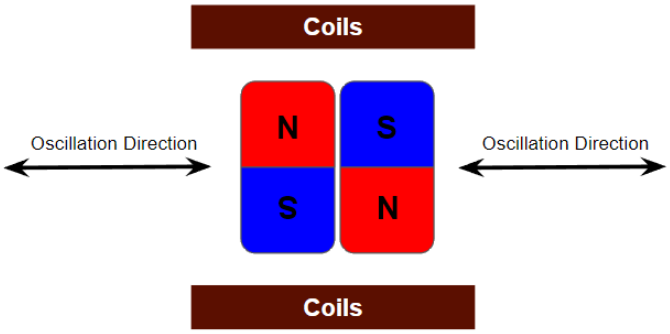

Figure 3-1: The side view of the harvester that shows two block magnets attach to each other.

greater change in magnetic flux compared to having one magnet that changes the flux from one value to another nonzero value with the same sign. Having more than two magnets, however, is not necessarily better. With careful sizing of the individual magnets, the change in flux density may increase with more magnets, but also leads to the induced voltage that is not sinusoidal. For the output electrical current to be directly useful in the power electronics, the induced voltage should resemble a sinusoid as closely as possible for efficiency. Therefore, having two magnets of the same size to form a block of magnet leads to the most desired induced voltage.

The exact dimensions of the individual magnets to be used for the harvester can be optimized to produce an energy harvester with the highest power density output, as defined by the output power divided by the total volume of the harvester. Using customized magnets from the potential optimization, however, is very expensive since manufacturers only mass produce for customized dimensions, when the assembly and testing of the design only require ten magnets at most. Further, the time it takes for the companies to produce custom sized magnets is too long. A decision has been made, therefore, to choose a commercially available magnet that is the closest to the dimensions derived from (2.8) considering the power requirement. Given the harvester size constraint as well as the need for a strong and dense magnet, for maximal power generation, N42SH block magnets of dimensions 1/4" x 1/8" x 1/16" are chosen. When two such block magnets are combined to form a magnet block as shown in figure 3-1, the dimensions of the block are 1/4" x 1/4" x 1/16", which translates to

6.35 mm x 6.35 mm x 1.5875 mm.

Now that the magnet size is chosen, the size of the coils of wires must be determined. The coils of wires are sized and placed so that the change in magnetic flux is the greatest while the magnets are oscillating. Therefore, the coils are place directly above and below the magnets. As the magnets sweep from one side to the other within the cavity of the harvester, the flux undergoes the most change right in the middle of the path where the magnets would lie without external vibration. Having excess of volume that extends past the specified footprint may at best provide marginal improvement in voltage output but potentially cause energy loss due to the wire resistance. The footprint of the wires are therefore approximately the same as the magnets', 6.35 mm by 6.35 mm. The actual coil of wires, however, will not be shaped like a block. Since the coils are wound manually, the resulting coils will resemble more elliptical in shape than a rectangle when viewed from above.

An analytic approach can determine the thickness of the coil windings, and therefore, the full dimensions of the coils. Consider Figure 3-1 again, redrawn in Figure 3-2, where the magnets have a known thickness T and the coils above and below the magnet block have the same thickness Δ. Further, the coils are sandwiched by thin pieces of back iron with high permeability that can complete the flux-path shown in yellow. The magnetic flux path describes the loop in which magnetic flux can travel through components of lowest reluctance. The air gap between the magnets and the coils should be as small as possible without the danger of the magnets scraping against the surface of the coils as they oscillate. For simplicity, this gap is assumed to be negligible.

If we draw a loop as shown in Figure 3-2, Ampere's law ensures that

$$H_M \cdot (2T) + H_g \cdot (4\Delta) = 0 \tag{3.1}$$

where H_M is the magnetic field in the magnets and H_g is the magnetic field in the coil volume between the magnets and the back-iron. Both H_M and H_g are assumed to be spatially constant for simplicity. Gauss' law further asserts that the magnetic

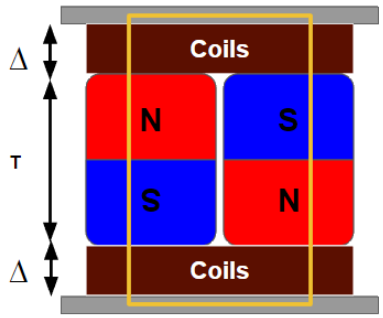

Figure 3-2: Ampere loop through the magnets, air gaps, and the back-irons.

flux density, B, must be continuous at the interface of the the magnets and the gap: $B_M = B_g$. The constituent relationship for the magnets is $B_M = \mu_\circ(M + H_M)$ while the constituent relationship for the gap is simply $B_g = \mu_\circ H_g$.

Solving the system of four equations together, the magnetic flux density can be expressed as $B = \mu_\circ M \frac{T}{T+2\Delta}$, where M is the permanent magnetization from the magnets. Then, the voltage produced by the magnetic fields is proportional to B and the number of turns N in the two coils: $V \propto B \propto \frac{T_\circ N}{T+2\Delta}$. The electrical resistance of the system comes from the coils of wire, so the resistance is proportional to N and inversely proportional to the thickness of the coils: $R \propto \frac{N}{\Delta}$. Then, the output electrical power is proportional to the following expression:

$$P \propto \frac{V^2}{R} \propto (\frac{T}{T+2\Delta})^2 \Delta \tag{3.2}$$

Note that power is not dependent on N. The power expression in (3.2) can be minimized when $\Delta = \frac{T}{2} = 0.8$ mm. If the coil thickness is too small, the shallow coils with less turns cannot generate enough voltage for harvesting to occur. On the other hand, if the coil is too thick, the large coil resistance as well as the lowered effective magnetic field experienced by the coils would lower the output power. This shows that the dimensions of the coils of wires should be approximately 6.35 mm by 6.35 mm by 0.8 mm above and below the magnets.

The amount of space dedicated to coils inside the harvester should be optimally utilized to produce maximum electrical power. An ideal winding structure produces

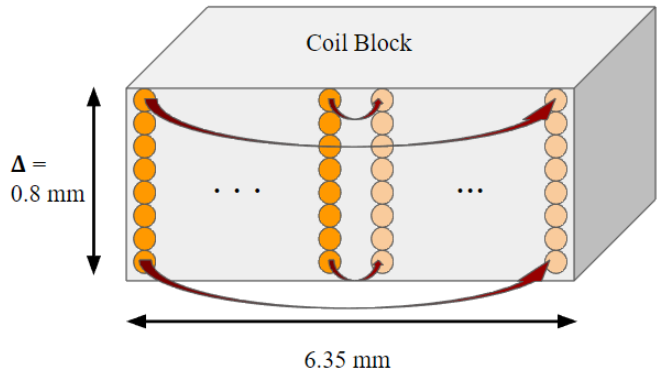

Figure 3-3: Winding scheme inside the coil block

sinusoidal output and is easy to manufacture. The ease of manufacturing is important for preliminary testing of the harvester since only a few coil blocks are necessary. Due to the small number of coils required, they are wound manually without a massive production from a manufacturer. Then, the harvesting scheme must be the simplest method for winding, which is producing a block of coil by winding a copper wire around a thin beam that has the height of 0.8 mm. Since the footprint of the coils is defined to be 6.35 mm by 6.35 mm, the wire gauge determines the number of turns required to produce a block of coil. To assess how many turns are required to produce sufficient electrical potential for the harvester circuit to function, static and dynamic analysis of the magnetics should be performed.

For a 39 AWG copper wire, the diameter is 0.09 mm. To fill a coil winding of volume 6.35 mm by 6.35 mm by .8 mm, the turns can fill up the space allotted for the coil winding as shown in Figure 6-3. Only eight wires can fit vertically within the space. Estimating how many wires can fit in the horizontal direction is trickier. When a coil is wound, the winding does not stay in a block shape but more resembles a elliptical cylinder. Making a conservative approximation that only about four-fifths of the coil block's length of 6.35 mm can effectively be used for winding, about 50 wires can fit horizontally. Therefore, $\frac{50}{2} \cdot 8 = 200$ turns comprises each coil block above and below the magnets.

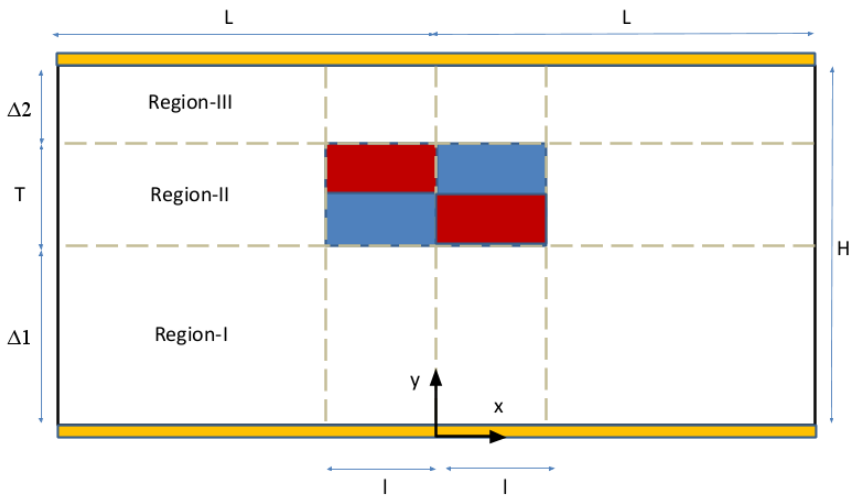

Figure 3-4: A simplified representation of the internal geometry of the harvester for electromagnetic analysis

3.2 Static Magnetic Analysis

The size and type of the magnets used in the harvester are already defined. Therefore, the magnetic field strength around the magnets should be analyzed before any calculation can be done to assess the voltage produced in a given winding of copper wires.

Figure 3-4 shows the setup of the static magnetic analysis. The x-coordinate is in the direction of the center-mass oscillation while the y-coordinate is in the direction corresponding to the thickness of the magnets and height of the harvester. The origin of this coordinate system is located at the top surface of the bottom back-iron just beneath the center of the magnet block. h represents the total internal height of the harvester, which is a sum of Δ_1, T, and Δ_2, which are the gap between the bottom back-iron and the magnets, the thickness of the magnets, and the gap between the top back-iron and the magnets, respectively. l is the individual length of each magnet while L is half of the internal harvester's length. In practice, Δ_1 and Δ_2 will be equal and most of the variables are already defined with a number in the sections leading up to this section. The analysis, however, is kept general to understand the effects of each individual variables in the resulting expressions.

The objective of the static analysis presented here is to determine the magnetic

vector potential around the magnets so that the magnetic flux through the windings can later be used in the dynamic analysis to calculate the voltage generated over one period of the magnet's motion. Since the self flux that leads to inductance is small, only the magentic flux generated by the magnets is considered. To begin, Ampere's law of the magnetoquasistatics Maxwell's equation in the differential form is expressed as

$$\nabla \times H = J \tag{3.3}$$

The relationship between the H field and B field in the presence of magnets is

$$B = \mu_\circ(H + M) \tag{3.4}$$

The relationships pertaining to the magnetic vector potential are derived from Gauss' Law, $\nabla \circ B = 0$.

$$B = \nabla \times A \tag{3.5}$$

$$\nabla \cdot A = 0 \tag{3.6}$$

Substituting (3.4) into (3.3),

$$\nabla \times (\frac{B}{\mu_\circ} - M) = J \tag{3.7}$$

$$\nabla \times B = \mu_\circ J + \mu_\circ(\nabla \times M) \tag{3.8}$$

Then substituting (3.5) into (3.8) yields

$$\nabla \times (\nabla \times A) = \mu_\circ J + \mu_\circ(\nabla \times M) \tag{3.9}$$

$$\nabla(\nabla \cdot A) - \nabla^2 A = \mu_\circ J + \mu_\circ(\nabla \times M) \tag{3.10}$$

$$\nabla^2 A = -\mu_\circ J - \mu_\circ(\nabla \times M) \tag{3.11}$$

There is no electrical current at the magnets or the back-iron. Therefore, (3.11) reduces to

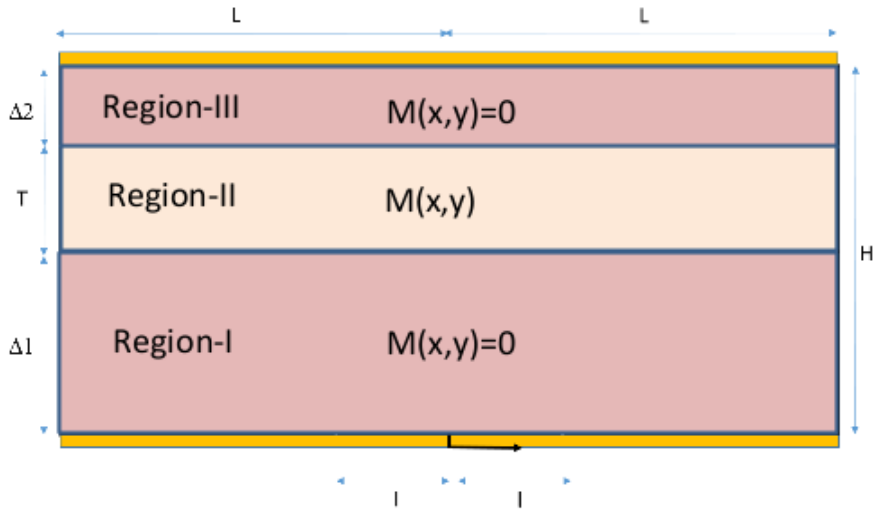

Figure 3-5: Internal geometry of the harvester divided into three regions, in which the magnets reside in Region II.

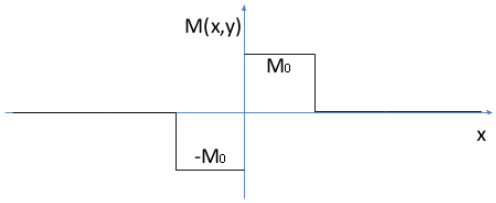

Figure 3-6: Plot of magnetization in Region II along x-axis.

$$\nabla^2 A = -\mu_\circ(\nabla \times M) \tag{3.12}$$

Important to note here is that (3.12) relates the magnetization and magnetic vector potential only in Region II of Figure 3-5 where the magnets reside. Regions I and III do not have any magnetization, so their analogous expression for the vector potential is

$$\nabla^2 A = 0 \tag{3.13}$$

Once the vector potential expression, A, is analyzed everywhere in the Regions I, II, and III, (3.5) is used to calculate the magnetic flux density everywhere in the harvester. The magnetization (M), however, is an aperiodic function without a closed form as shown in Figure 3-6. To analytically solve the expressions for vector poten-

tial, and in turn magnetic flux density, the magnetization function is decomposed to individual frequency components. Then, magnetic field can thus be calculated at the end by summing over all the spatial frequency components of the magnetic field expression.

Fourier analysis of the magnetization provides the following expression and its synthesis expression

$$M(x,k) = \int_{k=0}^{k=\infty} M_k \sin(kx)dk \tag{3.14}$$

$$\tag{3.15}$$

$$M_k = \frac{4M_0}{\pi k}\sin^2(\frac{kl}{2}) \tag{3.16}$$

Figure a) in Table 3.1 shows the original M function with two frequency components while Figure b) in Table 3.1 shows the plot of M_k versus the wave number.

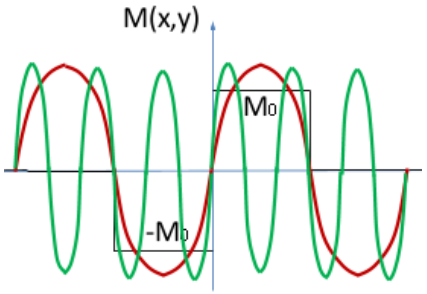

a) M function with two frequency components

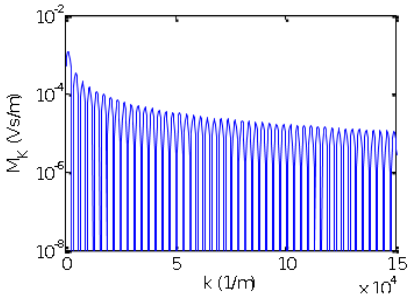

b) Plot of M_k, wave number, against k

Table 3.1: Frequency Decomposition of Magnetization

Now that we have the following closed form expression that relates magnetization to vector potential as in (3.17), boundary conditions must be defined to find the analytic expression for magnetic field and flux density inside the harvester. Therefore,

$$\nabla^2 A = \begin{cases} 0 & \text{for Regions I \& III} \\ -\mu_\circ(\nabla \times M_k \sin(kx)) & \text{for Region II} \end{cases} \tag{3.17}$$

At the interface between a back-iron and Region I, back-iron's high permeability

forces the x-component of the H field to be 0 such that,

$$\mu_o H_{1x}(y=0) = \frac{\partial A_1}{\partial y} = 0. \tag{3.18}$$

A similar expression arises at the interface between a back-iron and Region III,

$$\mu_o H_{3x}(y = T + \Delta_1 + \Delta_2) = \frac{\partial A_3}{\partial y} = 0. \tag{3.19}$$

At the interface between Regions I and II, tangential H and normal B should be continuous in x- and y-direction.

$$\mu_o H_{1x}(y=\Delta_1) = \mu_o H_{2x}(y=\Delta_1) = \frac{\partial A_1}{\partial y} = \frac{\partial A_2}{\partial y} \tag{3.20}$$

$$B_{1y}(y=\Delta_1) = B_{2y}(y=\Delta_1) = -\frac{\partial A_1}{\partial x} = -\frac{\partial A_2}{\partial x} \tag{3.21}$$

The same applies between Regions II and III.

$$\mu_o H_{2x}(y=\Delta_1+T) = \mu_o H_{3x}(y=\Delta_1+T) = \frac{\partial A_2}{\partial y} = \frac{\partial A_3}{\partial y} \tag{3.22}$$

$$B_{2y}(y=\Delta_1+T) = B_{3y}(y=\Delta_1+T) = -\frac{\partial A_1}{\partial x} = -\frac{\partial A_2}{\partial x} \tag{3.23}$$

One more important feature of the magnetic vector potential in the analysis is that the vector potential is nonzero only in the z-direction since the direction of motion is in the x-direction and the magnetization is in the y-direction. Taking advantage of this and the expressions (3.18) through (3.23), A(x,y) is solved for all three regions.

$$A(x,y)\hat{z} = \begin{cases} \frac{\mu_0 M_k}{k} \frac{\sinh((\Delta_1+T)k) - \sinh(\Delta_1 k)}{\sinh((T+\Delta_1+\Delta_2)k)} \cosh(ky)\cos(kx) & \text{for I} \\ \frac{\mu_0 M_k}{k} [1 - \frac{\sinh(\Delta_2 k)\cosh(ky) + \sinh(\Delta_1 k)\cosh((y-\Delta_1\Delta_2-T)k)}{\sinh((\Delta_1+\Delta_2+T)k)} \cos(kx) & \text{for II} \\ \frac{\mu_0 M_k}{k} \frac{\sinh((\Delta_2+T)k) - \sinh(\Delta_2 k)}{\sinh((T+\Delta_1+\Delta_2)k)} \cosh(ky)\cos(kx) & \text{for III} \end{cases} \tag{3.24}$$

These expressions can be confirmed by plotting their contour plots using MATLAB.

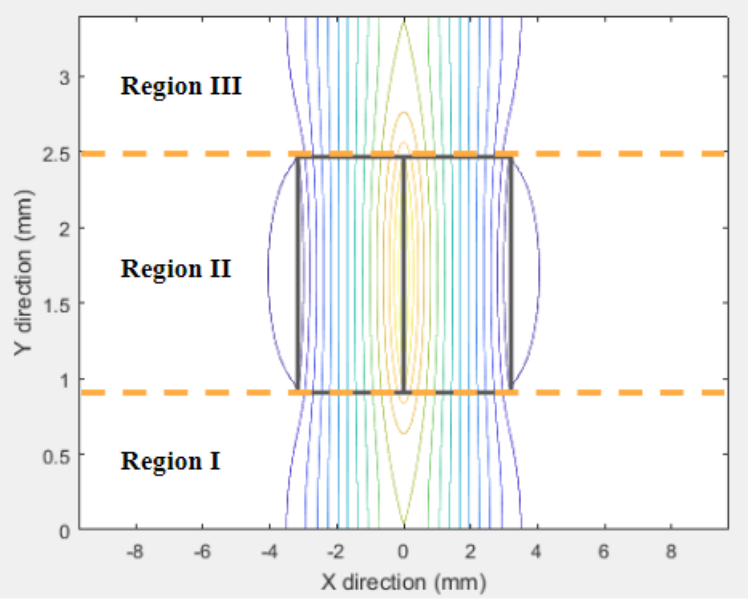

Figure 3-7: Contour plot of the z-component of magnetic vector potential, A.

The contour plot in Figure 3-7 shows the B vectors using 15 contour lines. The dimensions of magnets and air gap as well as the strength of the magnets are specified as determined in previous sections. Black boxes indicate the location of magnets, and the orange dashed lines show the division between Regions I, II, and III. The plot shows that the magnetic fields enter back-irons located at $y = 0$ and $y = \Delta_1 + T + \Delta_2$ perpendicularly. The contour lines are continuous and differentiable when transitioning from one region to another. The magnetic field inside the magnets is mostly straight, which justifies the original optimization. All these observations confirm that the vector potential expressions follow the boundary conditions, and the curl of the vector potential in (3.24) results in B_x and B_y, with $B_z = 0$.

3.3 Dynamic Magnetic Analysis

Now that the magnetic flux density around the magnets is characterized, dynamic magnetic analysis can be performed to determine how much voltage is expected to be generated with the chosen winding configuration.

The voltage generated by a coil is the derivative of the flux linkage with respect

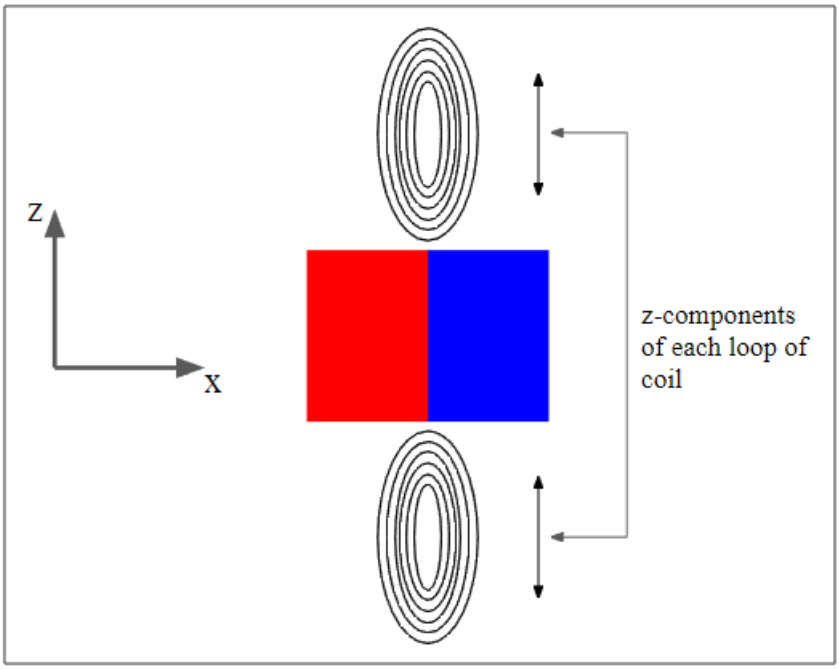

Figure 3-8: Side view of the inside of the harvester, with the z-components of each loop of coil indicated as two-headed arrows

to time: $V = \frac{d\lambda}{dt}$, where λ is the flux linkage. The flux linkage, in turn, is defined as,

$$\lambda = \int_S \vec{B} \cdot d\vec{S}, \tag{3.25}$$

where $\vec{B}$ is the flux density and S is the surface area defined by the coils through which magnetic flux passes. Substituting (3.5) into (3.25),

$$\lambda = \int_S \nabla \times \vec{A} \cdot d\vec{S}. \tag{3.26}$$

Then, Stokes theorem allows (3.26) to become the contour integral

$$\lambda = \oint_c \vec{A} \cdot dc, \tag{3.27}$$

where c is the winding path. As mentioned in the previous section, the magnetic vector potential is entirely in the z-direction. So, only the parts of the coil that are in the z-direction contribute to flux linkage. The side view of the harvester is shown in Figure 3-8, in which the z-components are indicated. In practice, multiple turns

form one continuous coil of windings, but each turn is analyzed as one loop of coil to simplify the analysis. Further assumption is made that the the z-component of each turn of the coil has the same length. With a simplification that the magnetic vector potential does not change in the z-direction and only depends on the x and y direction, (3.27) becomes

$$\lambda(x, y) = [A_1(x, y) - A_2(x, y)]l, \tag{3.28}$$

where A_1 and A_2 refer to the vector potential at each part of the coil that extends in the z-direction and l is the width of the magnets in the z-direction.

Applying (4.28) to the definition of voltage results in

$$V = \frac{d\lambda}{dt} = [A_1(x, y) - A_2(x, y)]l\omega. \tag{3.29}$$

(3.29) refers to the voltage produced by one turn of a coil. Finding a total open-circuit voltage requires summing over all the turns of the winding. As the center mass oscillates in steady state operation, only the x-coordinate of the coils change with respect to the magnets. The rate at which the x-coordinate changes is determined by the angular frequency of the oscillation as well as the maximum displacement.

Now that the voltage produced by individual loop of wires can be analyzed, all the individual electrical potentials can be summed to determine the total voltage that can be produced by the harvester. This method, however, only shows the amount of voltage generated at an instance in time. To view the voltage wave form over a period of oscillation, one period of time is divided into multiple samples. In each sample of time, the voltage is summed over all the loops of coil winding based on each loop's relative position with respect to the magnets.

The root-mean-square value of the voltage output is 80 mV when a conservative stroke length of 1.6 mm is used for calculation at 50 Hz. The coil resistance can be calculated by

$$R_c = \rho_c * (\text{total length of coil})/(\text{crossectional area of the wire}), \tag{3.30}$$

resulting in $R_c = 8.15\Omega$. The output power is, therefore, $P_{out} = \frac{V^2}{4R_c} = 390\mu W$, which is much higher than the target power output. The dynamic magnetic analysis shows that the energy conversion from internal kinetic energy to the electrical current results in plenty of power.

The above analysis, however, assumes that the center mass oscillates at a specific stroke length at a completely sinusoidal rate. Further, the output power calculated above utilizes open-circuit voltage. When a load is connected to the harvester to draw electricity, the power delivered to the load will be at most half the power derived from open-circuit voltage. Therefore, a full optimization analysis that combines the mechanics, electromagnetic, and load circuit will provide a more accurate estimate for the output power delivered to the applications that are powered by the energy harvester.

Chapter 4

Suspension Design

While completing the mechanical and electromagnetic analyses, the suspension type must be determined to begin optimization of the harvester design. Preliminary results from Chapter 2 demonstrate that the space inside the harvester should be used equally for the proof mass and the stroke (the space through which the proof mass travels through during oscillation). Further, the vibration of the proof mass should be parallel to the longest dimension of the harvester to maximize the output power. With this information in mind, the suspension scheme can be chosen from various options.

4.1 Suspension Types

Table 4.1 shows four different suspension types typically used for MEMS energy harvesting. While these devices have vastly different shapes and dimensions, the underlying mechanics of the operation is that the suspension moves a permanent magnet (or a coil of wire) around a coil of wire (or a permanent magnet) that is fixed to the casing to generate an alternating voltage by Faraday's law.

A cantilever beam suspension requires a long bending beam that is fixed to the harvester casing on one end while a proof mass, which can be a coil of wires or a permanent magnet, is attached to the other end of the beam. As the suspension vibrations, the cantilever beam bends in one specific direction. The proof mass, which is free to swing as the harvester vibrates, oscillates around a permanent magnet or a

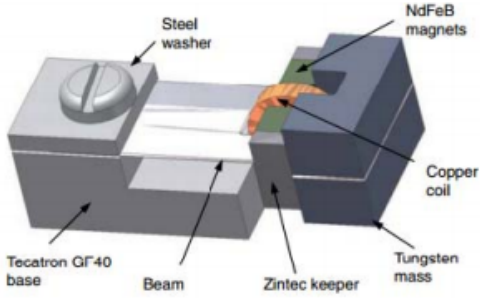

a) Cantilever Beam Suspension[3]

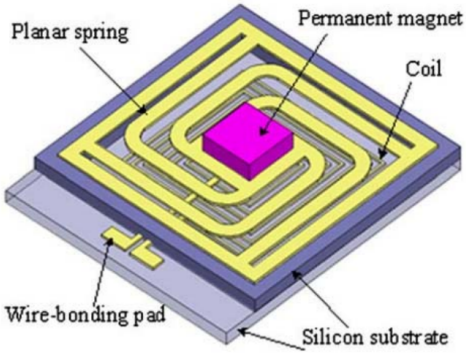

b) Planar Spring Suspension[7]

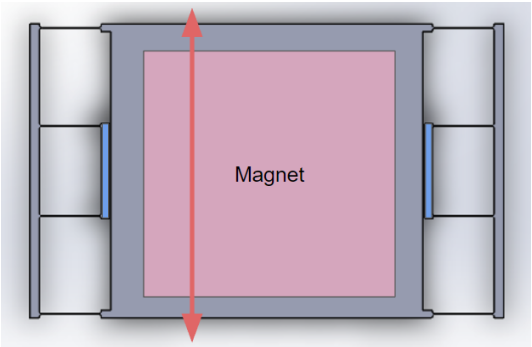

c) Four-Bar Linkage Suspension

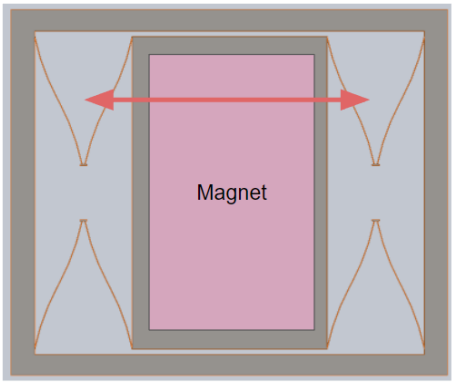

d) Accordion Spring Suspension

Table 4.1: Various Suspension Types

coil of wire that is fixed with respect to the casing. As a permanent magnet and a coil of wire oscillate with respect to each other, alternating voltage is generated inside the coil.

A planar spring suspension mounts a permanent magnet on a planar spring that can oscillate up and down as shown in b) of Table 4.1. A coil of wires are glued to the casing directly below the magnet. As the ambient vibration forces the magnet to oscillate vertically, the change in magnetic flux through the wires generates electrical current.

Figure c) of Table 4.1 shows the top view of a four-bar linkage suspension. In the figure, two narrow blue rectangles next to the permanent magnet are fixed to the casing of the harvester while the rest of the suspension is free to move. When the device vibrates, the bending beams allow the magnet to travel only in the direction

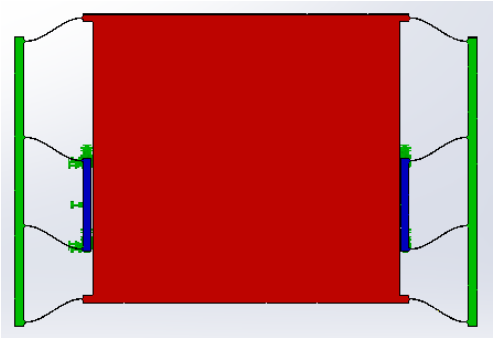

Figure 4-1: Four-bar Linkage Suspension with its Proof Mass Displaced

indicated by the double-headed red arrow. The thickness of the bending beams, which is not represented in the figure, prevents the proof mass from traveling in a direction not specified. To aid the visualization of how the bending beams deflect to allow the magnet to travel, Figure 4.1 is shown. Coils of wire are located above and below the magnet to generate electricity.

The last figure in Table 4.1 shows the accordion spring suspension. The magnet is attached to the casing by a pair of leaflet springs on both sides of the magnet. With ambient vibration, the proof mass oscillates in the direction shown in the red arrow. Similar to four-bar linkage suspension, coils of wire are located above and below the magnet to generate electricity.

Note that the suspensions depicted in Table 4.1 are only to help readers visualize typical suspension types, so the chosen suspension type will be optimized for the specifications outline in Chapter 1.

4.2 Choosing the Best Suspension Type

Now that four different suspension types are identified, the results from simplified analysis in Chapter 2 are used to find the best suspension type for the design of electromagnetic energy harvesters. The suspension types are compared purely based on whether each type satisfies the criteria that leads to maximum power output rather than comparing the expected power output of the optimized design for each individual suspension type.

The first criterion from the analysis is that the travel of proof mass must be in the direction of the longest dimension of the harvester. The cantilever beam suspension does not satisfy this criterion since the stroke of the proof mass at the end of the cantilever beam is necessarily a fraction of the length of the cantilever beam itself. Even if one attempts to increase the displacement of the proof mass using larger vibration amplitude, the mechanical strain on the bending beam will break the beam before the stroke length can surpass the length of the beam itself. This means that the direction of the stroke is not the longest dimension in a cantilever beam suspension. This suspension can be easily fabricated and assembled while being able to reject high modes, so this is more suitable for the design of suspension when the size constraint is not an issue.

By a similar argument, the planar spring suspension is not an ideal candidate for the project either. The advantage of a planar spring suspension is that the planar spring that surrounds the proof mass allows the mass to travel only in one direction while resisting any other motions, such as transverse, twisting, or rotating motions. As will be discussed later in this chapter, the specificity of the travel direction is important for efficiently translating external vibration energy into internal mechanical energy that can be used to produce electricity. The planar spring, however, requires the footprint of the spring to be larger than the stroke of the proof mass. Therefore, this suspension is not ideal for designing under size constraint, but is a good choice if the environment vibrates the harvester from many different directions with high amplitude.

The four-bar linkage suspension from Table 4.1 does not have a stroke length that is in the direction of the longest dimension. The maximum travel distance of the proof mass is determined by the separation between one of the outer bending beams and its adjacent inner bending beam as indicated in the yellow arrow in Figure 5-2. For the bending beams to be able to travel its maximum stroke, their lengths need to be at least three times as long as the stroke length. Then, the longest dimension of the harvester becomes the dimension in the direction parallel to the bending beams, which is perpendicular to the direction of the vibration. The four-bar linkage suspension,

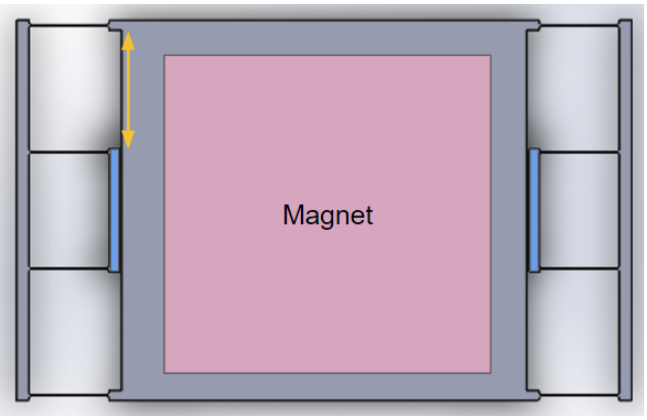

Figure 4-2: Four-bar Linkage Suspension with its Maximum Stroke Length Indicated

therefore, is not for the purpose of this thesis.

At last, accordion spring suspension is the only suspension type that can satisfy the above criterion. By design, an accordion spring is the simplest and is the most flexible of the designs since it only requires a pair of springs on either sides of the proof mass. Due to a specific structure to the design, the stroke direction can easily be the longest dimension of the device. The stroke can further be specified to be any fraction of the length of the harvester due to the design's flexibility.

4.3 Important Factors for Suspension

Aside from the two findings discussed in the last chapter, more factors must be considered to identify the best suspension scheme for the harvester. An ideal suspension is flexible enough to allow the device to utilize the entire volume of the harvester for travel and to have the resonance frequency of 50 Hz, while being strong enough to endure the stress that accompanies the oscillation. In addition, an ideal suspension's internal loss (mechanical or fluid friction) is minimal during operation. Starting from the decision to use the accordion spring suspension, the design should be modified to ensure that all of the above considerations are met.

4.3.1 Resonance Frequency

The resonance frequency, f_r, of a system is dictated by its mass and the spring constant by the expression, $f_r = \frac{1}{2\pi}\sqrt{\frac{k}{m}}$. For the accordion spring, whose mass of the center magnet dominates the mass of the silicon suspension, the magnet mass and the spring constant of the bending beam system control the resonance frequency. The magnet mass is determined by the size of the magnet, which is in turn determined by what is commercially available. Therefore, the spring constant of the suspension is the main independent variable that can be adjusted to arrive at the desired resonance frequency.

The spring constant of the accordion spring can be adjusted by changing the shape and dimensions of the bending beams that connect the proof mass to the casing of the harvester. The relationship between simple geometries, such as a rectangular beam, and spring constants has well been understood. The spring constant of a rectangular solid beam is directly proportional to $\frac{hw^3}{l^3}$, where l, h, and w are the length, height, and width of the beam. It is important to note here again that the width is in the direction of the magnet oscillation. Since all three of these parameters can be specified in design, the spring constant of the beams, and therefore the resonance frequency of the suspension, can be controlled.

Although the dimensions of the beams are flexible in concept, the practical requirements limit the range of possible dimensions of the beams. When fabricating the suspension by etching a silicon die, the minimum feature size refers to the smallest width a structure can be. At MIT's fabrication facility, this constraint is $15\mu m$. Therefore, the width of the bending beams cannot be arbitrarily decreased to reduce the resonance frequency. If the suspension must be stiffer, however, increasing the width can easily stiffen the beams.

On the other hand, the length of the bending beams is limited by the stroke length, or the size of the space between the casing and the proof mass. As the proof mass oscillates, the bending beams are squished in or pulled out rapidly. During this process the joint that connects the bending beams may collide against the casing of

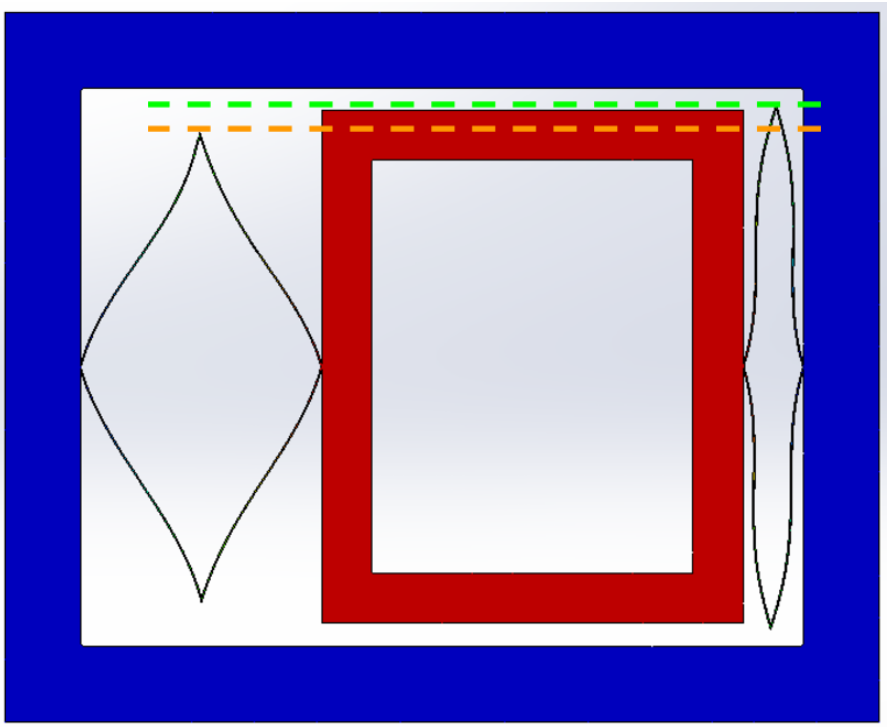

Figure 4-3: Contracting and Extending of Joints during Oscillation

the harvester. Figure 4-3 shows that as the proof mass oscillates, the leaflet springs contract and extend, leading a joint to extend further towards the casing. If such collision between any joints and the casing occurs, much of the internal mechanical energy is dissipated and the suspension is in the danger of breaking. To avoid this, the length of the bending beams must be shorter than the critical length at which the joint touches the casing when the proof mass has traveled its full stroke.

The height of the beams may be specified to further control the resonance frequency of the harvester. This adjustment, however, leads to a suspension that has more than one height throughout the device. In such a case, a complex fabrication process must be followed to introduce variability in height on the same silicon die. To reduce the complexity of fabrication and to reduce the cost, the height of the bending beams as well as the entire suspension can be specified to be the thickness of the silicon die before any processing. This leads to the height of the beams being a dependent variable that is dictated by the thickness of the silicon wafer.

4.3.2 Separation of Frequency Modes

The resonance frequency requirement only specifies how stiff the suspension should be in the direction in which the proof mass oscillates. The environment, however, does not provide an unidirectional vibration on its surroundings and rather vibrates its subjects in all directions with varying amplitudes. If any of the undesired movement modes are triggered by the external vibration, the suspension may oscillate in an unpredictable manner, which can make our harvester inefficient or for the center mass to carsh against the walls of the casing. Therefore, the resonance frequency of the harvester for all other modes must be sufficiently higher. Specifically, the higher modes must have frequencies that are higher than the second through forth harmonics (100 Hz to 200 Hz), so a safe minimum frequency set for the purpose of this project is 250 Hz.

To ensure the separation of frequency modes, a few modes with the lowest resonance frequencies are found. If the lowest mode frequency is not lower by a factor of 5 compared to the second lowest resonance frequency, the suspension should be modified to resist the motion that corresponds to the second lowest resonance frequency while keeping the lowest mode frequency, or the desired mode frequency, at 50 Hz. The frequency analysis described is conducted with Solidworks tool.

Table 4.2 shows the result of the frequency analysis for the accordion spring suspension shown in the previous section. Note that the tested model is not modified to operate at 50 Hz and instead has the resonance frequency of 102 Hz. (Iterations of frequency analysis have demonstrated that changing the resonance frequency by varying the dimensions of the bending beams does not change the ratio between the lowest mode frequency and second or third lowest mode frequencies.) Second and third lowest mode frequencies are 166 Hz and 223 Hz, which are too close to the desired resonance frequency. An inspection of the images show that the second movement mode corresponds to in-plane twisting of the proof mass. Given that the second lowest mode frequency is less than twice as big as the fundamental mode frequency, simply modifying the dimensions of the bending beams will not suffice.

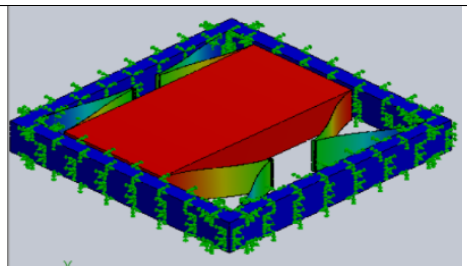 a) Lowest Mode of Accordion Spring (The desired mode)	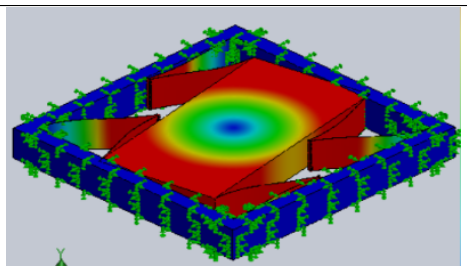 b) Second Lowest Mode of Accordion Spring (In-plane rotation)
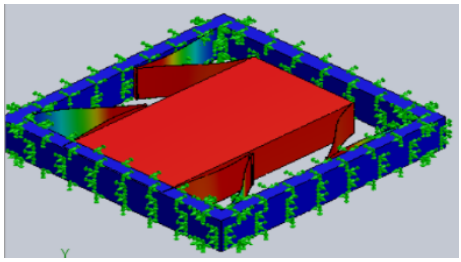 c) Third Lowest Mode of Accordion Spring (Out-of-plane rotation)	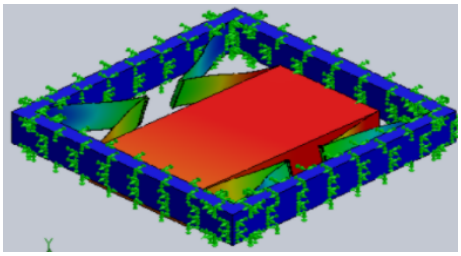 d) Forth Lowest Mode of Accordion Spring (Vertical displacement)

Table 4.2: Four lowest modes of movement for accordion spring suspension

Instead, side bars are added to the existing accordion suspension such that the joints of the bending beams are coupled. The side bars ensure that the coupled joints are separated by the same distance while the proof mass oscillates. The modification ensures that the suspension does not twist in-plane as easily as with the previous design. To demonstrate, the results of the frequency analysis of this design is shown in Figure 4-4. Lowest three mode frequencies are 51, 250, and 447 Hz. The second lowest mode again corresponds to in-plane twisting while the third lowest mode corresponds to out-of-plane translation. While in-plane twisting is still the second lowest mode, its frequency is now five times as high as the desired resonance frequency. Although some space inside the casing is used to include the side bars, their assistance with the separation of lowest modes makes the suspension a viable and robust design for the energy harvester.

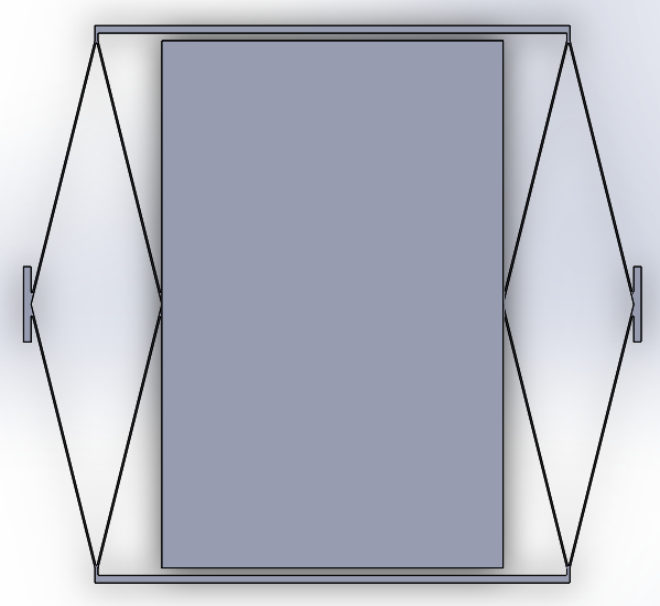

Figure 4-4: Accordion Spring with Side Bars

4.3.3 Mechanical Loss and Stress

The accordion spring suspension has been modified to ensure that the proof mass oscillates at the specified resonance frequency and only in the desired mode. To ensure the maximum transfer of energy from the external vibration to the internal kinetic/elastic energy, any source of energy dissipation should be minimized. The main ways in which energy can dissipate are internal mechanical losses.

To keep the internal loss low, the oscillation of the proof mass should not be retarded by surface friction or air drag. During operation, the proof mass may not be in contact with any internal structure that is not the suspension. If the proof mass brushes against any surface, the resulting friction drops the momentum of the center mass, adversely affecting the output power of the harvester. Even if the magnet does not suffer from surface friction, not having enough space between the walls of the casing and the magnet can result in air drag if the volume of air being displaced by the moving mass cannot escape due to the limited passage. Therefore, some empty space should act as a buffer between the proof mass and the inside of the casing.

The exact separation between the proof mass and the casing can be determined by calculating the smallest gap that allows the power lost from Couette drag to be

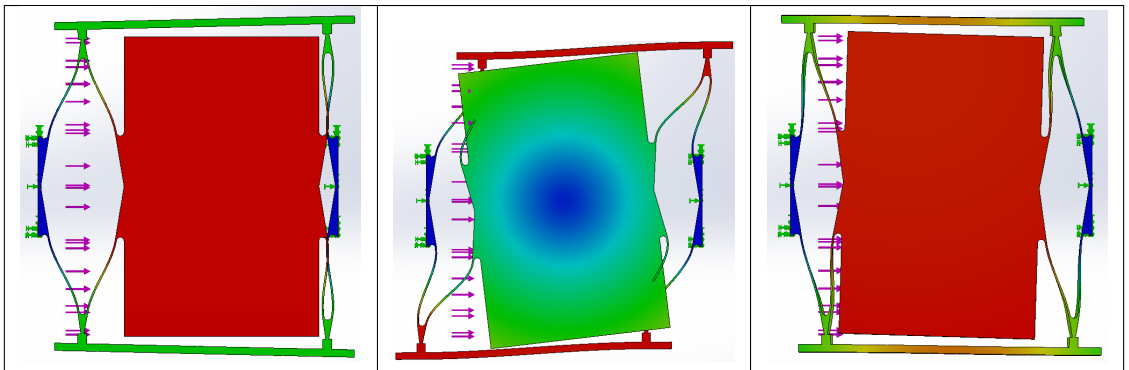

a) Lowest Mode	b) Second Lowest Mode	Third Lowest Mode

Table 4.3: Three lowest modes of movement for accordion spring suspension with side bars

significantly lower than the output power. To prevent the rubbing of the magents against the side walls, however, the air gap must already exist. Since this gap is sufficiently large, air drag is not a concern. The energy loss due to fluid damping is negligible compared to the amount of energy produced by the motion in the design.

Another source of energy loss is the device failure due to stress. As bending beams deflect to accommodate the oscillation of proof mass, the beams also stretch and contract. If the mechanical stress due to deflection, stretch, and contraction are too high, one of the beams will break, causing a catastrophic failure. To prevent this, the beams should be able to spread the stress over a larger volume so that the maximum stress is lowered. A bending beam shows the highest concentration of stress at the joints where the beam connects to a larger feature. Therefore, symmetric fillets are added to each end of all the bending beams. The radius all the fillets are approximately three times the width of the beams so that the stress at the end of a beam is sufficiently spread out. Further, the fillets are drawn to be symmetrical so that the stress is distributed evenly on both sides of the bending beam's joint, thereby preventing one side of the joint to have to endure a lot more stress than the other. Figure 4-5 shows the suspension with a close-up view of the symmetric fillets.

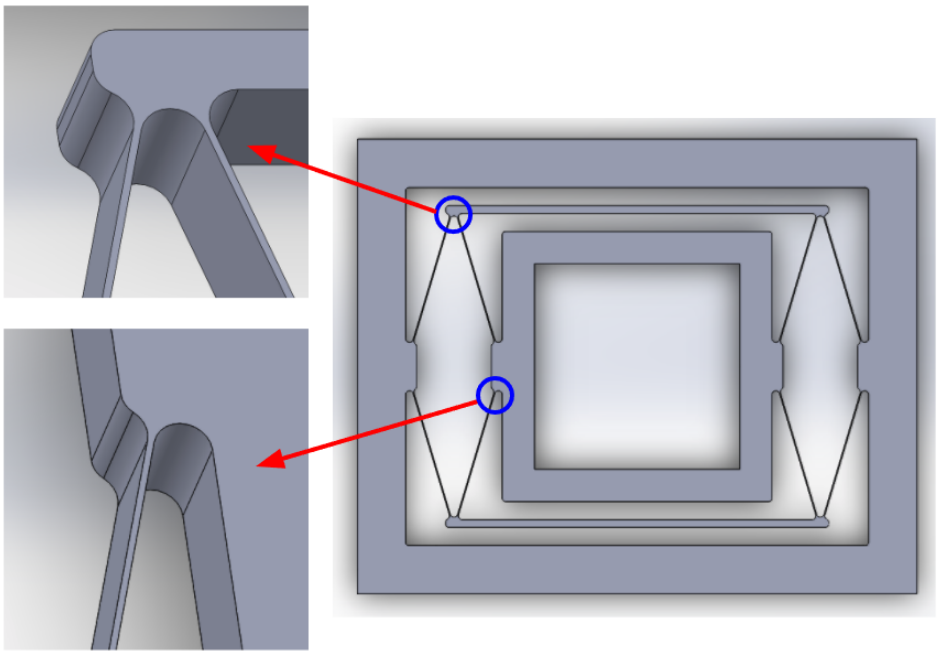

Figure 4-5: Modified Accordion Suspension with Close-up Views of Fillets

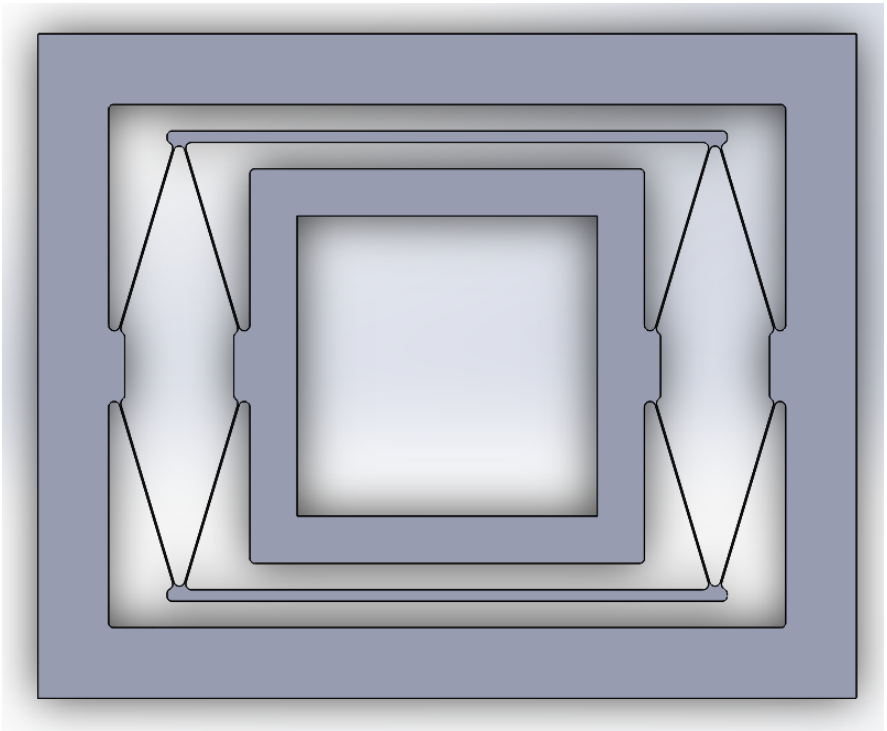

Figure 4-6: Modified Accordion Suspension with Side Bars

4.4 Suspension Design

The resulting suspension, that is designed to operate at 50 Hz only in the desired mode of movement without significant energy loss, is shown in Figure 4-6. This design shows the general shape of the suspension is not the final design. As mentioned in Chapters 2 and 3, a more detailed iterative optimization of both the mechanics and electromagnetics should be performed to determine the exact floor plan and size of the suspension.

Chapter 5

Full System Optimization

The chapters leading up to this one have described analyses that focus on the mechanics and magnetics of electromagnetic energy harvesters. Each topic is examined in isolation in previous chapters. Here, they are coupled to each other in practice. In this way, a full system optimization that incorporates all analyses can provide a better design for the harvester.[11]

5.1 Cross-Coupling Factor

Before combining different analyses together, important factors must be introduced and discussed. From the previous discussions, the effects of mechanics on the magnetism is clear: the suspension's ability to oscillate the center mass, or stroke length, and the magnetics dictate the voltage produced. When a load is connected to the harvester, however, the harvester is no longer operating in open-circuit, and the load impedance can influence the motion of the center mass. This co-dependence between the mechanics and the electrical of the harvester is expressed as the coupling factor "G".

This coupling factor, G, symbolically translates the internal kinetic energy of the

harvester into the electrical energy by,

$$Gu = V_o \tag{5.1}$$

$$Gi = f_c, \tag{5.2}$$

where V_o and u refer to the open-circuit output voltage of the coil and the velocity of the center mass, while i and f_c represent the output current and the mechanical force acting on the center mass. The conversion encapsulates a lossless Lorentz-force actuation that stores negligible energy in the coil inductance shown on the right side of the circuit. The energy conserving conversion is expressed as

$$f_c \cdot u = i \cdot V_\circ, \tag{5.3}$$

which is derived from multiplying (5.1) and (5.2) by i and u, respectively. This coupling factor allows the quantification of how the motion of the center mass affects the generated electricity as well as how the loading of the harvester circuit changes the output voltage, thereby affecting the motion of the center mass. G can also be thought of as the effectiveness of the coil configuration: a higher G value indicates that more voltage is produced given the same amount of motion from the magnets. The coupling factor can be approximated by performing a numerical simulation to find the electrical poential created based on the peak velocity of the center mass.

5.2 Circuit Representation of the Harvester

A circuit representation of the entire harvester system from the external vibration input loading can further assist the understanding of the coupling factor as well as the overall harvester operation. The circuit model is shown in Figure 5-1. Starting from the left side of the circuit, f is the sinusoidal external vibration force. B, M, and K are the internal damping factor, the mass of the center mass, and the spring constant of the harvester.

The circuit components to the left of the cross-coupled dependent sources rep-

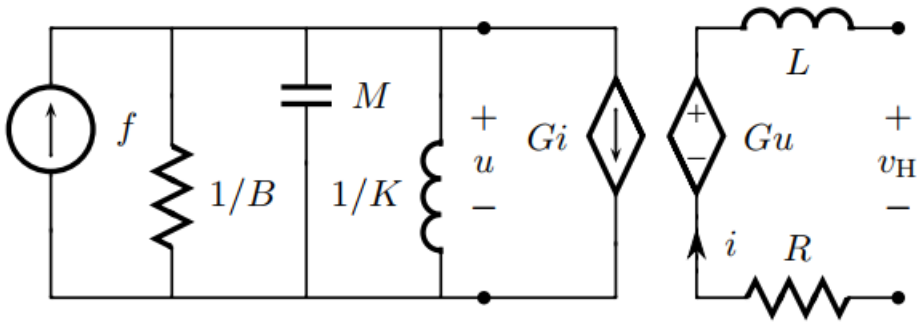

Figure 5-1: Open-circuit model of the electromagnetic energy harvester. Specific values for the variables can be derived from Table 5.1

resent the mechanical portion of the energy harvester. Each circuit component is appropriately labeled to ensure that the mathematics deriving from the circuit components reflect the physics of the mechanical properties of the harvester. For example, the motion of a harvester that is operating at its resonance frequency of $\omega_\circ^2 = \frac{K}{M}$ does not depend on its mass or spring constant. In the circuit representation, when the external force is operating at the same resonance frequency, the reactive components of the capacitor of value M and inductor of value $\frac{1}{K}$ cancel each other.

The right side of the dependent sources in Figure 5-1 show L and R that represent the parasitic inductance and resistance of the coil windings. The open-circuit voltage labeled v_H is the output voltage of the harvester.

The circuit model further facilitates the understanding of the conversion factor, G. As discussed before, G multiplied by u is the voltage equivalent of the mechanical side of the circuit and drives the current output. When examining the harvester in its open-circuit state, the output current is always zero even though the output voltage exists. This means that the current cannot feed back to influence the motion of the center mass. When a load is attached to the harvester to receive power, output current is generated by converting the mechanical power represented as $u \cdot (Gi)$ (which is equivalent to voltage times current) into electrical power, $(Gu) \cdot i$ (which, again, is voltage times current).

Now that the harvester model as a whole is understood and well-represented as a circuit, the model can be simplified to ease the analysis. When the dependent sources

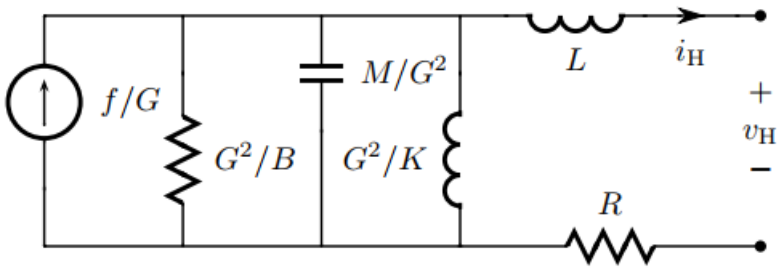

Figure 5-2: Simplified circuit model of the energy harvester.

are removed from the model, the circuit in Figure 5-1 transforms to Figure 5-2. The circuit components that represent mechanical properties of the harvester are modified to have values as seen from the output.

To further simplify the analysis, the parasitic inductance of the windings, which is represented as L, is ignored. The inductance is so small that the resulting time constant associated with the parasitic inductance is too small compared to the operating period. Therefore, the only remaining reactive components are the mechanical inductor and capacitor in parallel. These reactive components can be ignored when the device is operating at its resonance frequency. The external vibration, however, may not be operating exactly at the resonance frequency of the harvester. The designed harvester should be robust enough to generate enough power if the external vibration is within 5% of the device's resonance frequency. Therefore, full optimization is conducted with the reactive components to predict how the device may perform at 5% off-resonance.

5.3 Optimization Procedure

Optimization of output power involves many variables, some of which have already been determined. The variables that are already determined in the previous sections are the dimensions of the magnets and coils, the resonance frequency of the suspension, the internal damping factor, vibration amplitude, and the coil resistance. The variables to be optimized and determined are the length of a stroke and the load.

Assume that any arbitrary electrical load can be synthesized. This means that the

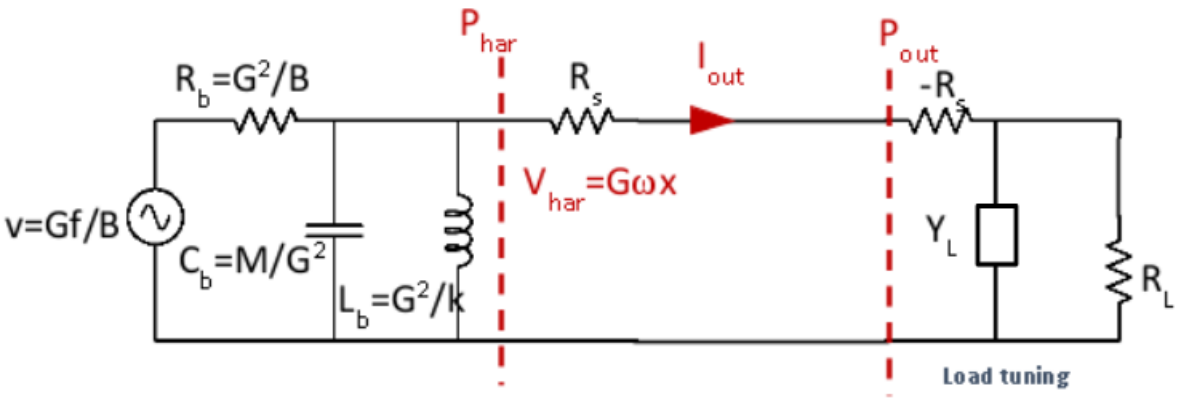

Figure 5-3: Further modified circuit model with a load.

load can be a combination of series and/or parallel circuits of reactive and resistive components. An arbitrary load can be achieved using a H-bridge circuit as the load (but the exact operation and the synthesis of the load will not be discussed in this thesis).[8] Then, the harvester circuit model can be loaded as shown in Figure 5-3.

The models shown to the left of P_{out} are the same as that in Figure 5-2, with a few exceptions. The parasitic inductance is removed from the circuit and the current source of the original model is replaced with a Thevenin equivalent circuit. The figure shows that $V_{har} = G\omega x = Gu$, which is the reiteration of Figure 5-1. Note that the analysis assumes sinusoidal steady state.

The synthesized load shown to the right of P_{out} is a negative resistor in series with a parallel circuit of a reactive component, Y_L, and a resistive component, R_L. This representation of the load is purely for analytic convenience, so load will not contain any component that has negative resistance. When the entire load is combined together to form an overall impedance, the real part of the impedance (the resistance) will be positive, so the load will sink power as intended. With this in mind, the negative resistor cancels out the parasitic coil resistance. Then, Y_L is in parallel with the reactive components from the harvester model. When the harvester is not operating exactly at resonance frequency, the combination of reactive components from the harvester model do not cancel each other. Therefore, Y_L is synthesized to cancel out any leftover reactive components, either capacitive or inductive, so that

Variable	Value
Resonance Frequency	50 Hz
Vibration Amplitude	.5 g = 4.9 m/s^2
Magnet Dimensions	6.35 mm ×6.35 mm×1.6 mm
Magnet Density	7500 kg/m^3
Magnetization	1.3 G
Internal Damping Factor	1.18×10^{-3} Ns/m
Wire Size	39 AWG
Winding Dimension	6.35 mm ×6.35 mm×0.8 mm
Number of Turns per Winding	200 turns

Table 5.1: Summary of variables needed to optimize the out power

maximum power transfer is achieved from the ambient vibration to the load. Finally, R_L matches R_b for maximum load power. With these implementation, the synthesized load can be characterized by the known variables.

The expression for power output contains all the variables discussed so far. Some of the variables are already defined with numerical values and are listed in Table 5.1. With the discussions leading up to this paragraph, the remaining variables can be expressed as known variables or the stroke length. Then, the power output expression can be rewritten to contain only one variable, the stroke length. Then, the partial derivative of the output power with respect to the stroke length can be equated to zero to find the optimal stroke length. The exact power output expression after all the substitution is a long and complicated expression that cannot be realized on paper. Therefore, MATLAB's symbolic representation tools are used to set up the optimization and solve for the optimal stroke length. Once the optimal stroke length is determined, the simulation calculates the expected output voltage as well as the output power for three cases: at resonance and at ±5% off resonance. The exact code for this procedure is attached as a part of the Appendix.

5.4 Optimization Results

Figure 5-4 shows the plot of output power with respect to stroke length. To generate this plot, the internal length of the harvester, which is the sum of the stroke lengths

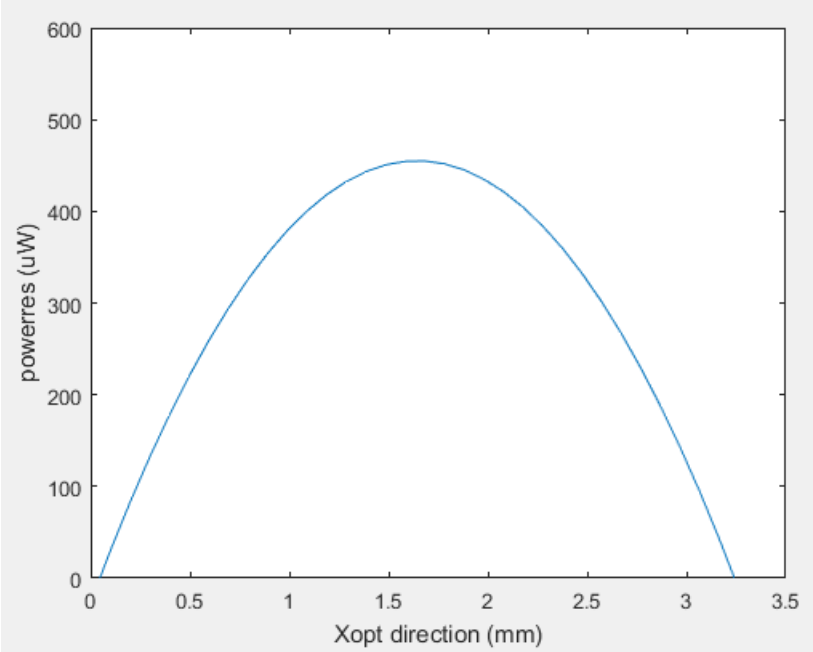

Figure 5-4: Plot of stroke length versus output power.

and the magnets' length, is fixed. The power decreases below 0 W above a certain stroke length because increasing the stroke length given the same internal length of the harvester forces the magnet length to decrease down to 0. Maximum power of 450 μW is achieved at the stroke length of 1.68 mm. The plot also shows that the the output power delivered to the load decreases quite rapidly as the stroke length increases or decreases from the maximum.

The power delivered to the load decreases at $\pm 5\%$ off resonance. When the device is operating at 47.5 Hz, which is 5% lower than the resonance frequency, the output power is 304μW. These values are determined based on a MATLAB simulation using the values shown in Table 5.1 and the optimal stroke length while varying the external vibration frequency. When the device is operating at 52.5 Hz, the output power is 320μW. Both of these power output are much higher than the minimum required output power, so the device is expected to function well even when the operating frequency does not exactly match the resonance frequency.

Additional plots of load voltage and load power versus frequency are shown within $\pm 5\%$ of the resonance frequency in the figures in Table 5.2. Unlike the plots for output power, the load voltage in the voltage plot drops quickly off-resonance. When the

device is operating off-resonance, electrical energy is exchanged between the reactive components of the mechanics and the reactive components of the load. Therefore, not as much voltage is dropped over the load resistance, resulting in a low load voltage.

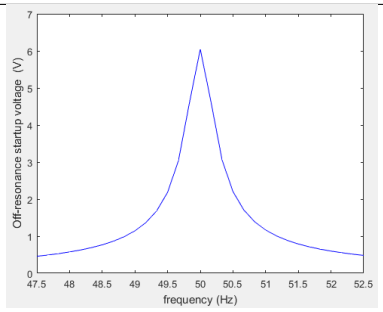

a) Plot of frequency versus load voltage

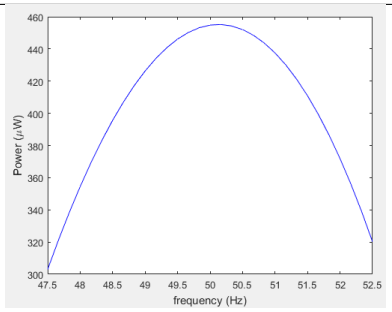

b) Plot of frequency versus output power

Table 5.2: Off-resonance Simulation Results

Full optimization that examines the coupled systems of mechanics and magnetism completes the design of the energy harvester. With the optimal stroke length as the main output, as well as all the variables defined in previous sections, the suspension and the coil windings can be produced for testing to confirm whether the suspension allows the center mass to achieve the optimized motion and whether the resulting electrical current provides the load power that is consistent with the findings of the simulation.

Chapter 6

Harvester Fabrication and Assembly

Following the completion of suspension design based on a full optimization of mechanics and electromagnetism, the suspension is fabricated and assembled to produce an electromagnetic energy harvester to be tested. This chapter details the fabrication process as well as the assembly and packaging of the suspension, coils, and 3D printed plastic parts, ending with a description of the full setup for testing.

6.1 Fabrication of Suspension

The suspension is designed with the ease of fabrication in mind. As discussed, the suspension has a uniform thickness of 550 microns to simplify the fabrication process by being compatible with halo etching. To perform halo etching, a layer of silicon dioxide followed by photoresist are deposited onto the silicon wafer.[9] A mask that has the shapes of the top of the suspensions is laid over the wafer, and the photoresist layer is exposed through the mask to imprint the shapes into the photoresist. The silicon die is then exposed to wet chemicals to etch through the parts of the silicon dioxide that are not protected by photoresist. Deep reactive ion etching is performed to finally etch through the rest of the silicon below the dioxide layer. The remaining product of the etching can then be removed from the process. If the suspension design does not have an uniform thickness, the amount and duration of the exposure must be tightly controlled to ensure the match between the product and the design.

The process of etching, however, cannot be closely controlled since the rate of etching varies during the process depending on the geometry of the design and the location across the wafer to be etched. Any attempt at controlling the depth of etching, therefore, leads to a varying degrees of etching for each suspension on the silicon die, thereby causing discernible variations across the suspensions that lead to different mechanical properties. Even though some of these variations still exist in halo etching, not having to control the amount of exposure in the process helps reduce the variations between suspensions on a die. One reason why simulating off-resonance performance of the harvester before fabrication is necessary is to ensure that the harvester will be functional even with 5% deviation from the resonannce frequency.

Another artifact of etching is the irregularity of the walls of the etched products due to blowout. As etchants etch down the parts of the silicon die that are not protected by photoresist, the etchant can etch the sidewalls of the suspensions, which are not deposited with photoresist. This phenomenon leads to the internal walls of a die to cave inwards. The phenomenon known as blowout is not a problem for sturdy structures, but the optimized suspension requires fabrication of thin bending beams of width less than 30 microns. Since the resonance frequency and the sturdiness of the suspension are sensitive to variations in the width of the bending beams, the beams must be designed to be wider to account for the blowout that will occur during fabrication. After iterations of experiments and experiences in etching, the fabrication facility at MIT has found the blowout size to be 2 microns per side wall when etching through 550 μm. Considering that a beam suffers the blowout from both sides, the beam is designed to be 4 microns thicker than the optimized design. For simplicity of drawing the suspension on SolidWorks, only the bending beams are widened to account for the blowout.

Once the design of a suspension is complete, the layout of the die is created to indicate which parts of the photoresist layer over the silicon die will be exposed. To maximize the utility of a silicon die of diameter 22 cm, multiple copies of the suspension are placed on a die, one next to another. Accounting for a die saw that

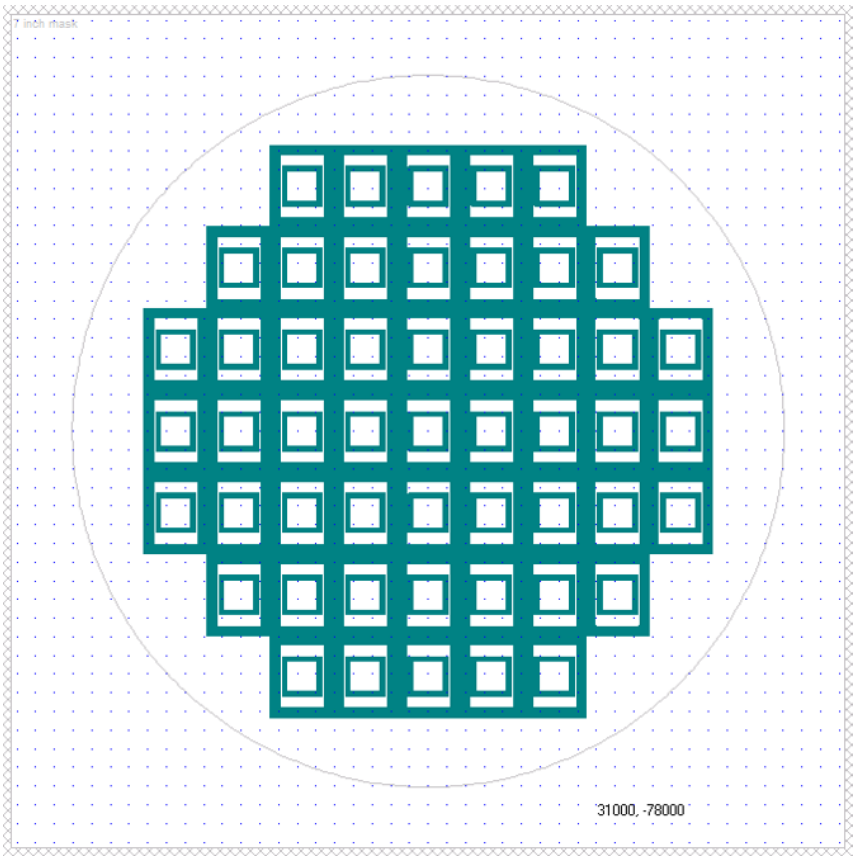

Figure 6-1: Placement of suspensions on a silicon die with a diameter of 22 cm.

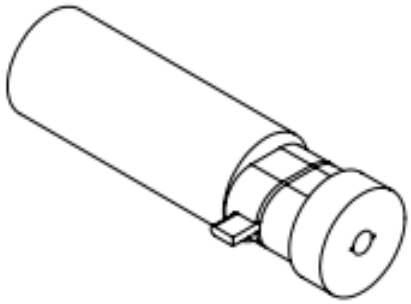

Figure 6-2: Wire holder that is attached to a lathe to wind a coil.

will be used to separate one suspension from another in an array of suspensions, a suspension on the die is separated from each neighboring suspensions by 100 microns. The layout of a silicon die accounting for the above considerations are shown in Figure 6-1.

6.2 Winding Coils

Aside from the suspension that holds the magnets, coil windings are essential in transforming internal kinetic energy into electrical energy. Electromagnetic analysis has shown that a winding of laminated 39 AWG copper wire is optimal for fitting as many turns of the wire into the space above and below for alternating current generation without resulting in the coil resistance that is too large for power output. A laminated copper wire is chosen specifically for insulation so that wires that are in contact with each other are not shorted.

To maximize the efficiency of the power generation, the coils must be tightly wound together and held in place so that the windings do not move with respect to each other during the oscillation of the center magnet. To do so, the wire must be wound at a slow and steady pace to ensure a tight packing using a lathe attachment (or a wire holder). A wire holder has an 800 micron gap with a column in the center around which the coil is wound. The picture of the wire holder is shown in Figure 6-2.

Figure 6-3: A coil of wire with each ends attacked to a cylinder for fixture.

To begin the winding process, one end of a wire is fed through the allotted slot, which is then covered by a small cover piece. The wire holder is then attached to a lathe that is configured to rotate at approximately 1 to 1.5 rotations per second. The cap is then closed on the wire holder to ensure an 800 micron gap and the winding begins. The winding of coils is done by manually feeding in the wire while holding the wire with a tight tension to pack the coil as densely as possible. While the copper wire is winding, a Gorilla liquid glue is applied every 20 to 30 turns to fix the turns in their places. When the winding is complete and the glue is dry, the cap of the wire holder is carefully removed to avoid damaging the wire. Then, the cover piece for the wire feeding is taken out with a tweezer and the winding can be separated from the wire holder. Throughout the process, the wire can be damaged, ruining the whole winding. To avoid this, some acetone is applied to the interface between the winding and the wire holder to dissolve some of the glue. Care must be taken to carefully control the amount of acetone used since excess acetone can dissolve the glue that holds the winding together. To ease this process, the wire holder is made of Teflon, a polymer plastic that does not adhere well to the glue.

The resulting coil of wire is then soldered on both ends to expose the conductive portion to be connected for measurement or power electronics. The final product is shown in Figure 6-3. Since the coil is wound manually, some variations are introduced for different windings, resulting in varying overall footprint. As long as the number

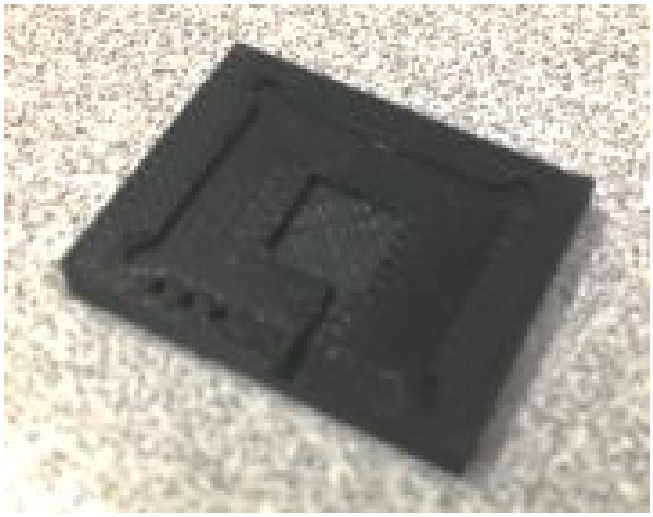

Figure 6-4: Gluing platform for attaching the magnets to the suspension.

of turns are the same, however, the variance in the power of produced alternating current is low.

6.3 3D Printed Assembly Parts

After the fabrication of the suspension and the winding of coils, all components must be packaged together to form a harvester. For quick production of the parts necessary to package the components, a 3D printer is used to print the parts with plastic.

Before assembling the parts, the magnets must be fixed inside the frame of the suspension. To assist with this process, the plastic gluing platform shown is Figure 6-4 is printed. The gluing platform is designed so that the suspension can fit snugly inside the frame cavity while the center of the platform is lowered to fit a pair of magnets. When the magnets are inserted inside the frame of the suspension and touch the floor of the gluing platform, the center of the magnets coincides with the center of the suspension. Then, super glue is applied around the side of the magnets so that the magnets are glued to the frame of the suspension.

To connect the coils with the suspension and center mass, three additional printed plastic parts are used. Figure 6-5 shows three different plastic parts that encase the suspension as well as two coils. The suspension sits inside the middle plastic part

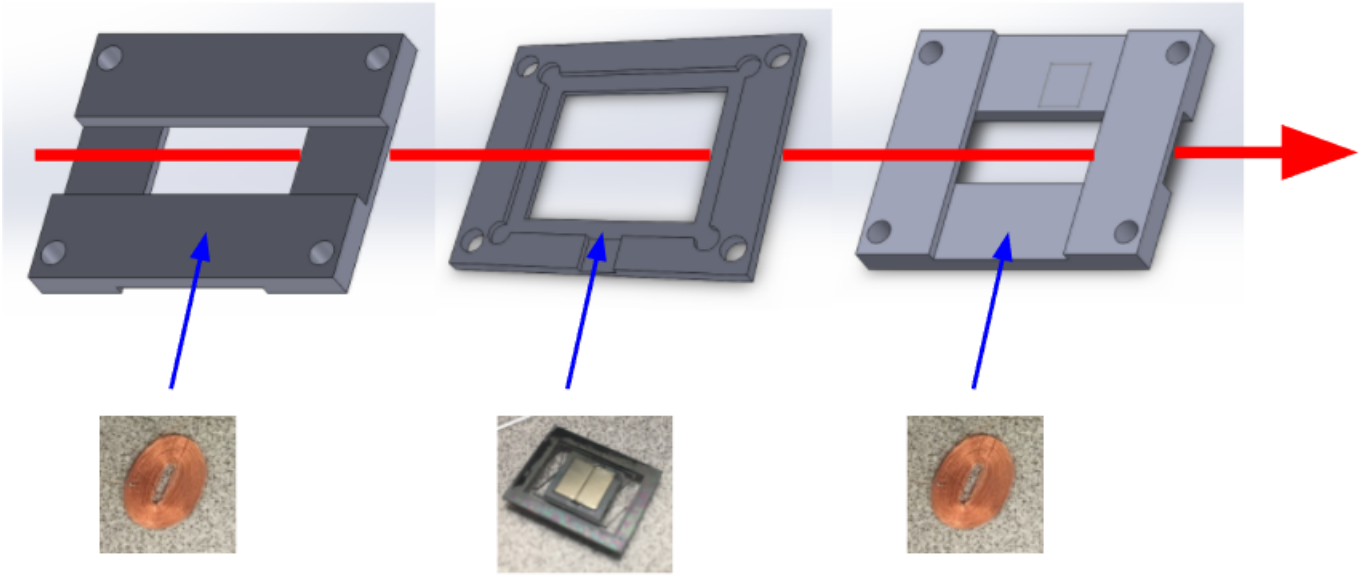

Figure 6-5: Three plastic printed parts that need to be combined along with the suspension and two coils to assemble into a harvester. Note that the top and bottom parts of the assembly each have an additional horizontal slot for backiron.

while two coils of approximately 200 turns are glued to their respective slots in the top and bottom plastic parts. Then, some candle wax is dropped onto the outer frame of the suspension to ensure that the suspension is fixed to the plastic part. The three plastic parts are attached to either the suspension or a coil of wires and are shown in Figure 6-5.

When combining the three harvester parts together, paper shims are inserted between the parts to control the separation between the coils and the center mass. The magnets and the coils ideally need to be as close as possible to create a greater change in magnetic flux, but they need to be far enough apart so that the danger of the magnets scraping against the coils of wire is eliminated.

With the individual components ready, the harvester must be coupled with a vibration source that can simulate an external vibration. The vibration platform shown in Figure 6-6 has a cylindrical base with four holes to fix to the vibration source and a plank protruding from the top with a cavity where the harvester sits. This cavity has another set of four smaller holes through which a screw can enter to fix all three parts of the harvester.

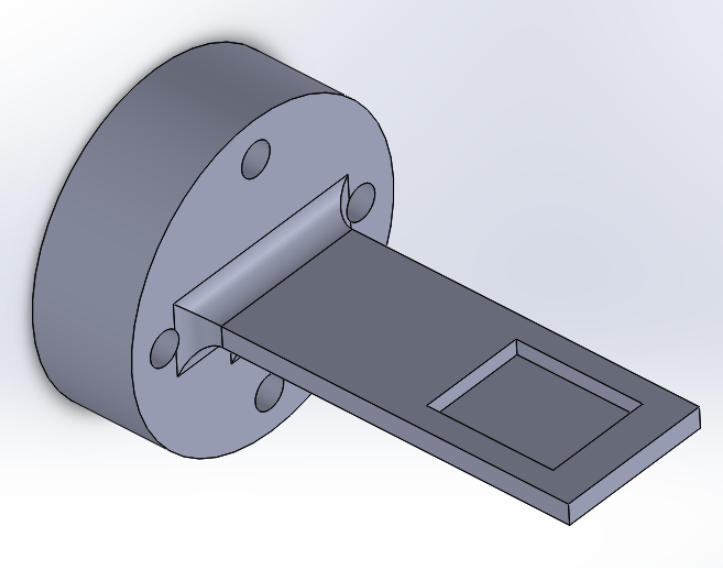

Figure 6-6: Vibrating platform that connects to the mechanical vibrating machine.

Fully assembled harvester attached to the vibrating source is shown in Figure 6-7 and is ready to be tested.

Figure 6-7: Fully assembled harvester on a vibrating platform that is connected to the mechanical vibration machine.

Chapter 7

Tests and Results

The device must be tested to determine whether the experimental data matches the simulated data. If the harvester does not operate or produce power as expected from the analysis, additional simulations and tests are performed to identify the sources of discrepancies.

7.1 Testing Procedures

For testing, the shaking platform containing the assembled harvester is attached to the mechanical vibrating machine as shown in Figure 6-7. An accelerometer is attached to the shaking platform to observe the vibration amplitude of the artificial external vibration. The end turns of the coil windings are connected in series to form an open-circuit configuration. Open-circuit voltage can be measured directly from the end turns of the coils with an oscilloscope. A load comprising of a simple resistor may be connected to the end turns to estimate the power output while the harvester is operating at resonance frequency. Remember that a reactive component is also required at the load to maximize the delivered power when the device is not operating exactly at resonance as established in Chapter 6.

To determine the actual resonance frequency of the system, the open-circuit rms-voltage with respect to frequency is measured. The open-circuit voltage is measured as mentioned above each time the frequency is increased in increments of 0.1 Hz while

keeping all other conditions constant. As the frequency sweep is performed starting from a frequency well below the target resonance frequency of 50 Hz, the actual resonance frequency of the harvester is detected when the voltage begins to decrease as the frequency continues to increase. The frequency continues to be increased until the open-circuit voltage becomes small does not decrease much further. Then, the same analysis can be repeated with the frequency decreasing from above the measured resonance frequency. If the frequency response is symmetric around the resonance frequency, the device is in smooth operation. If a clear imbalance between the two responses is apparent, nonlinear deflection of the suspension is suspected and further testing and/or simulation is required to understand the problem.

Another important property that can be measured from the open-circuit voltage testing is the quality factor of the device. Given that the frequency response is symmetric around the resonance frequency, the frequencies that lead to the open-circuit voltage that is $\frac{1}{\sqrt{2}}$ of the voltage at resonance are estimated and used to calculate the quality factor using the equation $Q = \frac{f_r}{\Delta f}$ where f_r is the resonance frequency and Δf is the difference in half-voltage frequencies. This quality factor can assist in better understanding how sensitive the device is to deviations from resonance.

Using a purely resistive load with varying resistance, the power output can be estimated. At or near resonance, the reactive behaviors of the suspension can be ignored, and the harvester can be approximated to have a purely resistive source impedance. As the load resistance is varied while all other conditions are kept constant, the load voltage can be measured to calculate the output power delivered to the load. Iterations of this experiment are performed until a specific resistance that leads to the maximum power output is determined. That resistance is approximately the sum of the wire resistance and the resistance that represents the internal damping of the device. Therefore, the internal loss can also be estimated as well as the maximum power output at resonance with a purely resistive load.

7.2 Results

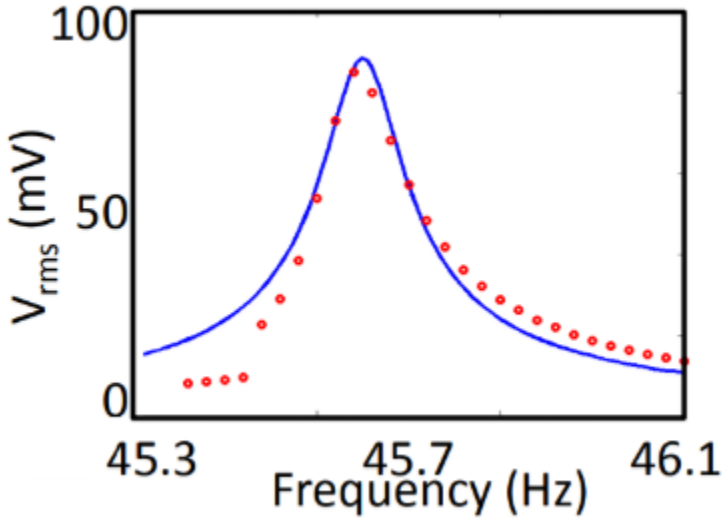

Figure 7-1: Frequency versus RMS Voltage Plot with a Blue Line indicating Simulated Result

Preliminary measurements show that the coils have a combined resistance of $R_{coil} = 16\Omega$. This confirms that the coil resistance is quite low, but this value must be compared against the effective mechanical resistance.

The frequency sweep of rms open circuit voltage measurements is shown in Figure 7-1. The general shape of the plot is a sharp bell-curve that is skewed to the left. If the data was plotted on a log-log scale, the shape will more closely resemble that of a Gaussian curve. The plot shows that the maximum rms voltage is achieved at 45.6 Hz, which represents the resonance frequency of the harvester. The suspension was designed to have its resonance frequency at 50 Hz, so the result fits within 5% of the target frequency. A result from the experiment is that the observed stroke length of the device is much lower than the expected stroke length at about 0.8 mm. This resulted in a much lower voltage output than expected from the results in electromagnetic analysis. The blue tracing in the plot shows the simulated results using the same parameters as the experiment except setting the resonance frequency of the device to be 45.6 Hz and approximating the stroke length to be 0.8 mm. This result shows that the experimental data is well-predicted by the simulation, especially

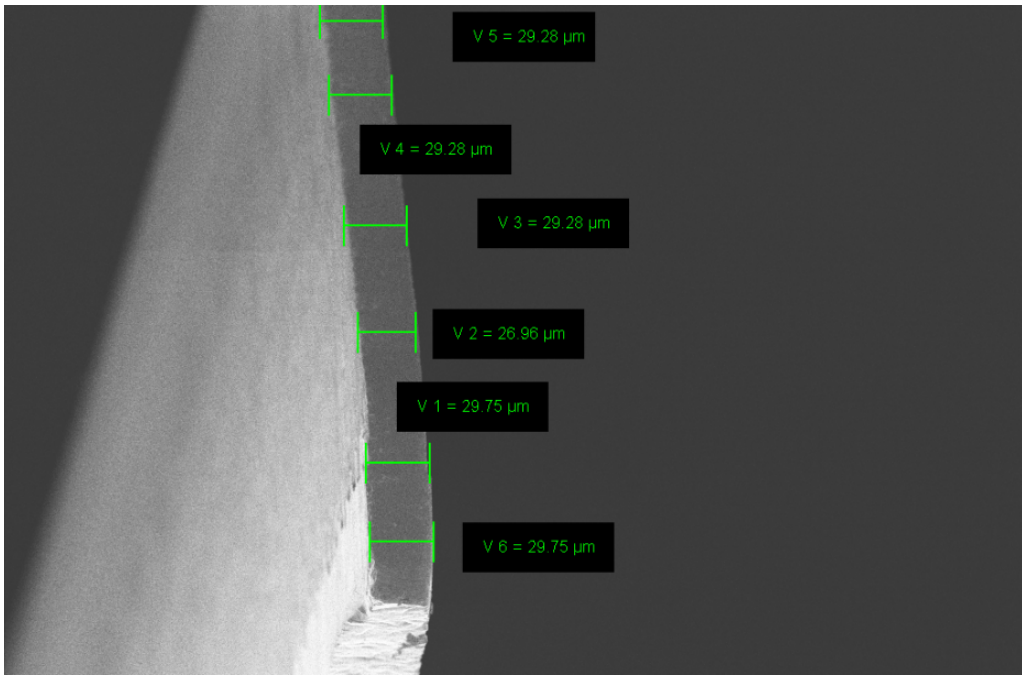

Figure 7-2: Scanning Electron Microscope Image of a Bending Beam of the Suspension

for higher frequencies.

Among many factors that may contribute to the deviation from 50 Hz, the fabrication variabtion is the most probable. Therefore, a scanning electron microscope (SEM) was used to capture images of the suspension beams, the structures whose variation would affect the resonance frequency the most. Then, SEM image was compared with a scale to identify the width of a bending beam at multiple points along its height. The width of the beam is shown to be approximately 29.28 microns on average in figure 7-2. The suspension was designed to have bending beams of width 28 microns to resonate at 50 Hz using COMSOL integrated simulation. Since various parameters entered into the software, such as Young's modulus, are variables that cannot be easily predicted without experiments, the simulation results are expected to deviate from ideal calculations. The fact that the device's resonance frequency is within 5% of the target frequency is impressive.

The quality factor of the harvester is approximated using $Q = \frac{f_r}{\Delta f}$ where f_r is the resonance frequency and Δf is the difference in half-power frequencies. In Figure 7-1, the resonance frequency is 45.6 Hz while the half-power frequencies are at 45.55 Hz and

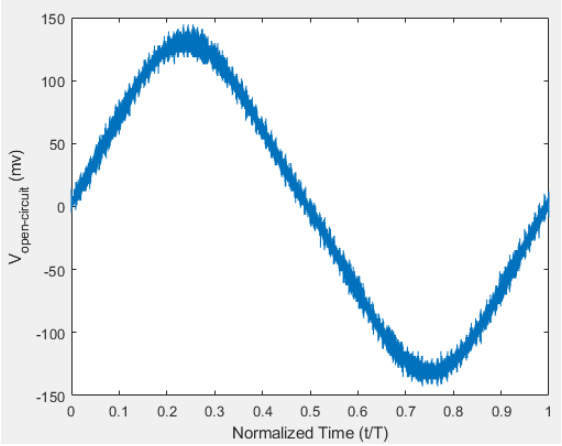

Figure 7-3: Open-Circuit Voltage of the Harvester over One Period at a=0.4g and the Stroke Length of about 0.8 mm

45.67. The quality factor is therefore $Q = \frac{45.6Hz}{45.67Hz-45.55Hz} \approx 380$. This confirms the assumption that the quality factor is high enough to isolate the resonance frequency response to produce a sinusoidal voltage output, which is shown in Figure 7-3.

The coupling factor, G, and the damping factor, B, are approximated using experimental data. $G = \frac{V_o}{u} = \frac{V_o}{2\pi f_s \bar{X}} = 0.524$, where the open-circuit voltage is derived from Figure 7-3 and the operating frequency is 45.6 Hz. $B = \frac{2\pi f_s M}{Q} = 0.0004$, where the magnet mass is calculated from Table 5-1 and the quality factor of 380 is used. Using these values, $R_B = \frac{G^2}{B} = 688\Omega$. This shows that the mechanical damping dominates the coil resistance.

To estimate the optimal load resistance for maximum power delivery, discrete resistors of various resistances were connected to the harvester at low acceleration. In such case, the optimum load resistance R_L at resonance is matched to be $R_{coil} + R_B$, the sum of coil resistance and mechanical damping of harvester, and found to be 1100Ω. The empirically determined total resistance is much greater than the calculated total resistance of $688\Omega + 16\Omega = 704\Omega$. Given that the stroke length and quality factor are estimated values, the results are not too far from each other. At low acceleration, the stroke length is not big enough to be visually approximated, so neither the coupling factor nor the mechanical damping can be calculated. At a higher acceleration, past 0.4 g, the bending beams of the suspension broke consistently

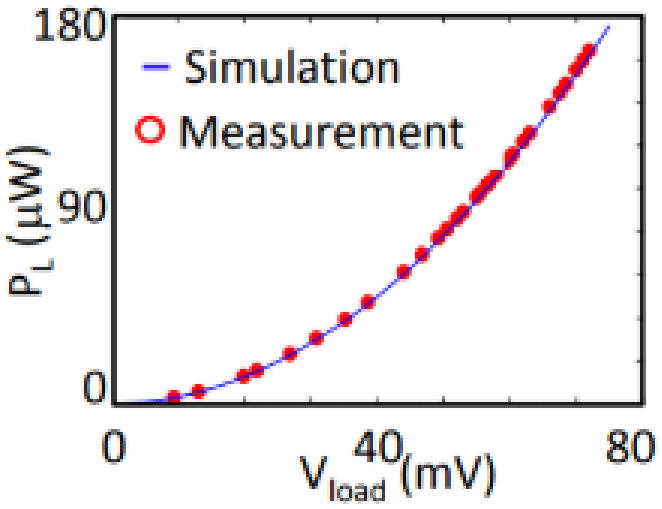

Figure 7-4: Load Voltage versus Power Delivered to Load using $R_L = 16\Omega$

at resonance, preventing the harvester from achieving the full stroke. To maximize the power delivered to the load at a high a=0.4 g, a coil-load matching condition of $R_L = R_{coil} = 16\Omega$ is connected at the output. Since the device is operating at a linear region away from the optimal loading condition to prevent the device from breaking, N With $R_L = 16\Omega$ fixed, the acceleration is increased starting at the acceleration of 0.015 g to plot the load voltage against power delivered to load in Figure 7-4 and to plot the acceleration against power density in Figure 7-5, where power density refers to the load power.

Below the threshold acceleration at which the suspension breaks, the harvester is operating in its linear region as evident by the trend. To estimate the power delivered to the load, $P_L = \frac{V_{ptp}^2}{8R_L}$ is used to plot Figure 7-4. Maximum load power of $165\mu W$ is delivered at acceleartion of 0.4 g. Increasing the acceleration past 0.4 g leads to the catastrophic breaking of the bending beams of the suspension. To compare the performance of the harvester to reported MEMS-based harvesters that have varying sizes, the power density of the harvester is calculated by dividing the load power by the active volume of 0.43 cm^3 (1 cm· 1.3cm· 0.33 cm), the volume occupied by the suspension. The resulting power density is plotted against the external acceleration in Figure 7-5. The highest power density is calculated to be 382 $\mu W/cm^3$.

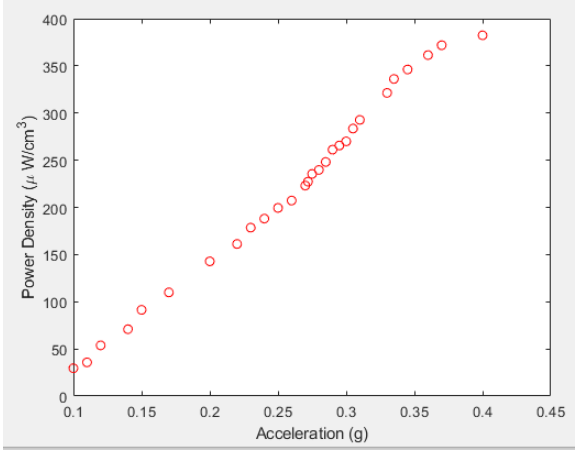

Figure 7-5: External Acceleration versus Power Density at 0.4 g Acceleration using $R_L = 16\Omega$

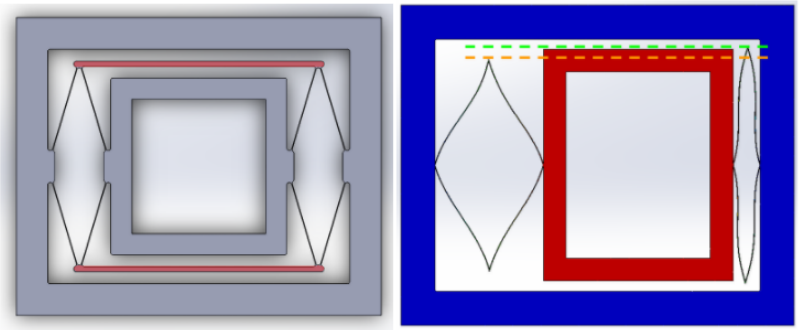

Figure 7-6: a) The Suspension with Sidebars Highlighted in Red. b) Bending Beams' Exaggerated Movement as Indicated by Dashed Lines.

The measured power of $165\mu W$ exceeds the initial goal to design a harvester that delivers more than $100\mu W$, but this result is much lower than the simulated results that predicted the output power to be approximately $450\mu W$. This discrepancy comes from the inability of the suspension to operate linearly at 0.5 g acceleration. Even though the suspension is designed to oscillate with the stroke length of 1.6 mm, the bending beams break when the stroke length exceeds 0.8 mm. Since the power output is highly dependent on the stroke length of the harvester, the power output is much lower than expected.

Upon a closer inspection at the mechanics of the suspension design, the side bars, as indicated in red in Figure 7-6 a), are preventing the full deflection of bending beams. These bars are added to the design to separate the frequency modes of

the desired mode of movement from other modes. Although the bars are useful in restricting the movement of the suspension in the desired direction, they also force the distance between the two joints to be the same throughout the oscillation since the bars cannot be extended length-wise. In Figure 7-6 b), an exaggerated picture of the suspension while it has traveled to one side, the distance between the joints is at least 5% higher than when the suspension is at rest. Since the side bars, which are fabricated from silicon dioxide, cannot be stretched rapidly to accommodate for the suspension's travel, the bending beams break before the desired stroke length is achieved by the harvester.

Table III of Y. Tan et. al. summarizes the performance of state-of-art MEMS-based harvesters.[2] The highest reported power density among the devices shown in the table is $222\mu W/cm^3$. Since the maximum power density achieved by the harvester presented in this thesis is $382\mu W/cm^3$, the design is still competitive without achieving its full stroke length, and thereby producing much higher power density.

Chapter 8

Conclusion

8.1 Summary and Conclusions

The goal of the thesis has been to design, fabricate, assemble, and test an electromagnetic energy harvester that may be used with a diverse types of applications. The context and goals as well as specifications for the device is outlined in the introductory chapter. The motivation behind investigating an efficient MEMS-based vibrational harvester as well as the systemic overview of the conversion from vibration internal electric energy are outlined. The aim of this thesis is specifically to design a harvester that operates at 50 Hz while producing optimal output power of at least 100 μW under the influence of 0.5 g acceleration. For the deisgn to be integrated with other MEMS devices, the volume of the harvester is restricted to be 1 cm^3 at maximum. Then, the design space is narrowed to a design of Lorentz-force electromagnetic energy harvester due to the low resonance frequency and relative ease of fabrication using silicon die.

Chapter 2 introduces a preliminary optimization of the dimensions associated with mechanical parts of the harvester. With a classic spring, mass, and damper system coupled to ground by suspension, the analysis of the model's steady-state oscillation shows that the mass of the center mass, external acceleration, resonance frequency, and stroke length are equally important in producing the largest electircal power. Further analysis by decomposing the center mass into dimensional components reveals

that the direction parallel to the oscillation must be in the direction of the longest dimension of the harvester. Due to the need for a dense proof mass as well as the ease of assembly, the center mass is determined to be a block of neodymium magent (NdFeB) oscillating between coils of wire fixed above and below the magnet. Many simplifying assumptions made in the preliminary optimization calls to question the accuracy of the analytic expressions shown, but the analysis is still intrumental in qualitatively prioritizing the important aspects of the mechanical design.

Chapter 3 presents electromagnetic analysis that is used to determine the configuration and sizing of electromagnetic components and to approximate the amount of electrical energy that can be harvested from the components. For optimal energy generation, two neodymium magnets of size 1/4" x 1/8" x 1/16" are attached together to form the proof mass of size 1/4" x 1/4" x 1/16". An analysis using Ampere's law shows that the approximate coil windings to be fixed above and below the magnets must have the dimensions of 1/4" x 1/4" x 1/32", which translates to 200 turns of 39 AWG copper wire. Further analysis using Maxwell's Equations reaveals that the oscillation of the harvester with the stroke length of 1.6 mm leads to the generation of 80 mV of root-mean-square voltage output to the coils, which collectively have the resistance of 8.15 Ω. In such scenario, the output power is estimated to be 390 μW. Although the final design of the harvester may not allow the proof mass to oscillate by 1.6 mm, the electromagnetic analysis can be integrated with mechanical analysis to produce a better estimation.

Chapter 4 presents and evaluates several suspension schemes that may be used for the harvester. The harvester's suspension must be designed to provide 50 Hz resonance frequency, allow the stroke length to be large, and separate the freqeuncy of desired mode of movement from other modes'. Both accordion suspension with side bars and four-bar linkage suspension satisfy each of the criteria. To allow for a certain fixed stroke length, however, the footprint of four-bar linkage suspension must be at least three times as large as that of an accordion spring. Since the size constraint on the harvester is of grave concern, the accordion spring with side bars is chosen for hte harvester. To reduce stress on the bending beams of the suspension

and therefore reduce the mechanical loss, appropriately sized fillets are placed at or near all the joints of the suspension.

Chapter 5 integrates the results from mechanical and electromagnetic analyses to estimate the output power from the harvester. A circuit abstraction of both the mechanical and electrical components of the harvester is produced using a cross-coupling factor that allows the energy conversion between mechanical power and electrical power. A fully integrated circuit model of the harvester is then used to determine the optimal stroke length of 1.68 mm and the associated power output of 450 μW. The analysis shows that the output power will exceed the goal of 100 μW as long as the oscillation achieves the desired stroke length and the internal power loss is minimal as predicted.

Chapter 6 outlines the fabrication and assembly of all the parts of the desgined harvester. A general overview of halo etching technique used to produce the suspension from silicon die is presented along with undesired artifacts that is likely to affect the design parameters, such as resonance frequency. The method of manually winding coils and the design of associated tools are shown as well. 3D plastic printed parts are then deisgned and produced to assemble the harvester and to fix it to an exteranl vibrating source. The printed plastic parts functioned well as the assembling parts to the harvester. The most challenging part of the assembly is the manual winding of the coils, which requires many repetitions of winding in case the coil is not tightly wound or is woundly so tightly that the wire breaks.

Chapter 7 details the testing procedures and reports the corresponding results of the harvester. The open-circuit voltage of the harvester at various operating frequencies is measured to determine the resonance frequency of 45.6 Hz as well as the quality factor of about 380 for the device. By varying the resistive load to the harvester, the maximum output power is measured to be 165 μW, with its power density calculated to be 382 μW/cm^3. Overall, the experiment data matches the simulated data quite well. The result may be better predicted if the software is utilized well with more accurate material property parameters to predict the resonance frequency of suspension designs. The measured maximum output power is much lower than the

predicted output power because the harvester is not able to achieve the desired stroke length. This can be improved if the device can be designed to achieve the desired stroke length. In any case, the power density of the design is well above the power density reported from other MEMS-based harvesters.

8.2 Future Work

While the energy harvester designed and tested in this thesis meets the power requirement of 100 μW, the device has the potential to achieve a much higher power output, and therefore power denstiy output. Since the side bars of the accordion suspension, which are added to provide modal separation, are preventing the proof mass from travel the desired distance during oscillation, the design may benefit from removing the side bars. With the measured quality factor of about 200, the frequency response of the suspension shows a well-isolated peak at its resonance frequency, so the device may oscillate only in the desired direction without the side bars.

Another option is to redesign the suspension using a four-bar linkage suspension. The accordion spring is chosen over the four-bar linkage configuration due to having a larger required footprint for a given stroke length. If achieving a higher output power is a priority to the size constraint, a four-bar linkage suspension is competitive and must be explored. Its associated modal separation as well as the connection of the bending beams ensure that this design is more likely to achieve the full stroke without unexpected pitfalls.

References

[1] D. P. Arnold. *IEEE Transactions on Magnetics*, vol. 43, no. 11, pp. 3940-3951, Nov. 2007.

[2] Y. Tan et. al. *Journal of Microelectromechanical Systems*, vol. 26, no. 1, pp. 1-16, Feb. 2017.

[3] S. P. Beeby et. al. *J. Micromech. Microeng.*, vol. 17, no. 7, p. 1257, 2007.

[4] J. M. Gilbert and F. Balouchi, "Comparison of energy harvesting systems for wireless sensor networks" in *Int. J. Autom. Comput.* vol. 5, no. 4, pp. 334-347, Oct. 2008

[5] G. Poulin et. al. |Generation of electrical energy for portable devices: Comparative study of an electromagnetic and a piezoelectric system," *Sens. Actuators A, Phys,* vol. 116, no. 3, pp. 461-471, 2004.

[6] J. Pyrhonen et. al. *Design of Rotating Electrical Machines*. John Wiley and Sons. 2009.

[7] P. Wang et al. "A micro electromagnetic low level vibration energy harvester based on MEMS technology," *Microsyst. Technol.,* vol. 15, no. 6, pp. 941-951. 2009.

[8] J. Bowden et al. "Synthesizing Load Impedance to Freqeuncy-Tune an Electro-Mechanical Vibration Energy Harvester" in *24th Conference on Mechanical Vibration and Noise* 2012.

[9] R. Ghodssi et. al. *MEMS materials and processes handbook*, Springer, 2011.

[10] C. T. Pan et. al. "Fabrication and analysis of a magnetic self-power microgenerator," *J. Mag. Magn. Mater.,* vol. 304, no. 1, pp. e394-e396, 2006.

[11] J. H. Lang, *Harvesting energy at multiple vibration frequencies*, unpublished, Massachusetts Institute of Technology.